University of Stavanger

Faculty of Science and Technology

MASTER'S THESIS

Study programme/ specialisation: M.Sc., Petroleum Technology/ Natural gas	Spring semester, 2018 Open
Author: Kenneth Edgar Boultwood Nergård	..... (signature of author)
Programme coordinator: Jann Rune Ursin Supervisor(s): Dhruvit Satishchandra Berawala, Pål Østebø Andersen	
Title of master's thesis: Investigation of Geomechanical Effects and Other Controlling Parameters on Shale Gas Production	
Credits (ECTS): 30	
Keywords: - Shale gas production - Fracture-matrix modelling - Geomechanics in shale gas reservoirs - Stress-dependent formation - Dimensionless numbers	Number of pages: 56 Stavanger, 15.06.2018

Acknowledgements

I would like to acknowledge my two supervisors Dhruvit Satishchandra Berawala and Pål Østebø Andersen for their excellent guidance and assistance throughout the work on this master's thesis.

Abstract

Shale gas reservoirs are mainly characterized by their low matrix permeability, ranging from sub-nanodarcies to tens of microdarcies, which makes the economic production of these reservoirs rare without needing artificial stimulation. However, developments within two major technologies, horizontal drilling and hydraulic fracturing, have made the production more viable and shale gas reservoirs have attracted a lot of interest from around the world. Because of their abundance, shale gas reserves can provide part of the solution to the world's growing energy demands. In conventional reservoirs, Darcy's law is typically used to model the gas flow. However, gas flow in shale gas reservoirs is more complicated than in conventional reservoir because of many coupled processes such as gas adsorption and desorption, a large gas slippage effect (Klinkenberg effect), strong rock/fluid interactions and geomechanical effects. The impact on flow behaviour from these mechanisms is currently not well understood and although there are a few shale gas simulators available, they do not comprehensively involve all of these mechanisms.

In this thesis, an investigation of geomechanical effects and other controlling parameters for shale gas production is undertaken using a mathematical 1D+1D shale gas flow model. The model was provided by Berawala et al. (2018) and has been extended to include geomechanical effects. Geomechanical effects can be included into reservoir modelling by treating porosity and permeability of the formation is stress-dependent properties. Since the incorporation of geomechanical effects changed the scaling of the model, the new scaling approach has also been part of the thesis work. The model involves a high-permeable fracture extending from a well perforation through symmetrically surrounding shale matrix with low permeability. A sensitivity analysis is performed where geomechanical effects are varied in addition to varying other reservoir properties such as the fracture size, fracture shape, fracture spacing and initial reservoir pressure. Input parameters from literature data are applied. The simulation results are interpreted with and without using the dimensionless numbers α and β. The value of can express $\alpha\beta$ the residence time of gas in the fracture compared to in the matrix. Therefore, if $\alpha\beta \ll 1$ it is expected that fracture properties have little impact on gas recovery.

Table of contents

Nomenclature

Roman:

a_g	=	Adsorbed gas, kg/m^3
a_{max}	=	Max capacity adsorbed gas, kg/m^3
$\hat{a}_g$	=	Adsorbed gas, Pa
$\hat{a}_{max}$	=	Max capacity adsorbed gas, Pa
b	=	Fracture half-width, m
b_0	=	Average fracture half-width, m
b_{max}	=	Max half width (at well), m
b_{min}	=	Min half width (at end of fracture), m
b_g	=	Inverse gas volume factor, -
h	=	Fracture height, m
K	=	Absolute permeability, m^2
P_g	=	Gas pressure, Pa
P_L	=	Langmuir half capacity pressure, Pa
T	=	Temperature, K
V	=	Volume, m^3

Greek:

η_m	=	Matrix porosity-stress-dependence factor, Pa^{-1}
μ_g	=	Gas viscosity, $Pa\ s$
ρ_g	=	Density, kg/m^3
ρ_{gs}	=	Surface gas density, kg/m^3
σ'_m	=	Mean effective stress, Pa
τ	=	Time scale of diffusion, s
ϕ	=	Porosity, -
Ψ_f	=	Fracture permeability-stress-dependence factor, Pa^{-1}
Ψ_m	=	Matrix permeability-stress-dependence factor, Pa^{-1}

Indices:

atm	=	Atmospheric conditions
f	=	Fracture
$init$	=	Initial conditions
m	=	Matrix
$well$	=	Well conditions

Abbreviations:

GOIP	=	Gas originally in place, kg
GCIP	=	Gas currently in place, kg
TOC	=	Total Organic Content

1. Introduction

1.1 Shale Gas Reservoirs

1.1.1 General Background

Unconventional reservoirs can be classified as hydrocarbon-bearing formations in which economic production rates cannot be achieved without artificial stimulation. Shale gas, coalbed methane, tight sandstones and methane hydrates are all examples of such unconventional resources (Passey et al. 2010). The matrix permeability in shale gas reservoirs is very low and the existing natural fractures are usually not enough for attaining economic production rates. However, in recent years the interest in shale gas has increased dramatically because of the development of hydraulic fracturing technology. This technology, combined with horizontal drilling, makes economic production of shale gas possible. Moreover, since shale gas reservoirs are abundantly available throughout the world, they can provide part of the solution to the world's growing energy demands in the coming decades (Swami and Settari, 2012).

1.1.2 Characteristics of Shale Gas Reservoirs

Shale gas reservoirs are organic-rich shale formations which serve as both reservoir and source rock at the same time and can contain gas in adsorbed form in addition to free gas which is normally found in conventional reservoirs (Yu and Sepehrnoori, 2014). The term shale has been used to describe a wide variety of rocks that are mainly composed of extremely fine-grained particles that are typically less than 4 microns in diameter. Shales can therefore be classified as mudstones and exhibit a wide range of constituents (clay, quartz, feldspar, heavy minerals, etc.). A large variability in matrix lithology is observed when comparing shale formations found worldwide (Passey et al. 2010). The adsorbed gas found in shale gas reservoirs mainly lies on the surface of the shale matrix and in the organic matter (i.e. kerogen), while the free gas mainly lies in natural fractures (Yu and Sepehrnoori, 2014). The amount of adsorbed gas can be 20-80% of total gas reserves (Curtis 2002; Wu et al. 2014) and is dependent on the adsorption capacity of a shale, which is related to factors such as total organic content (TOC) and the specific surface area of nanopores (Wang et al. 2017). Nanoscale natural fractures act as pathways that can transport free gas and connect the low-permeability shale matrix (Wang et al. 2017).

The matrix usually has extremely low permeability that ranges from sub-nanodarcies to tens of microdarcies and varies depending on the shale type (Wang and Reed, 2009). At depths typical for oil and gas reservoirs, the porosity of shale formations ranges from 2 to 15% (Curtis, 2002). There are mainly two types of pores present in the matrix: nano-scale pores and micro-scale pores (Wang and Reed, 2009). The constituents that make up the pore structures in shale gas reservoirs can be divided into four types: organic material with high porosity, inorganic material that often has a high clay mineral content, natural fractures, and hydraulic fractures (Wang et al. 2017). Loucks et al. (2009) observed three main modes of nanopores occurrences in shale formations: within grains of organic material as intraparticle pores, between organic material patches (kerogen packets) as intraparticle pores, and in fine-grained matrix not associated with organic material. The use of high resolution scanning-electron microscopy (SEM) has suggested that there exists a separate porosity system contained mainly inside the organic matter of shales (Klimentidis et al. 2010; Loucks et al. 2009; Ambrose et al. 2012; Sondergeld et al.

2010). It appears that as much as 50% of the original volume of organic matter may consist of these pores in some shales. This means that the pore volume within organic matter may be a significant fraction of the entire porosity in some shale gas reservoirs. **Figure 1** shows an SEM photomicrograph of a fine-grained sandstone and compares it with the scale at which porosity is observed in organic matter in a Barnett organic-rich shale rock (Passey et al. 2010). These pore spaces range in size from 5 to 1,000 nanometers and are thought to have been formed when oil and gas was generated (Wang and Reed, 2009).

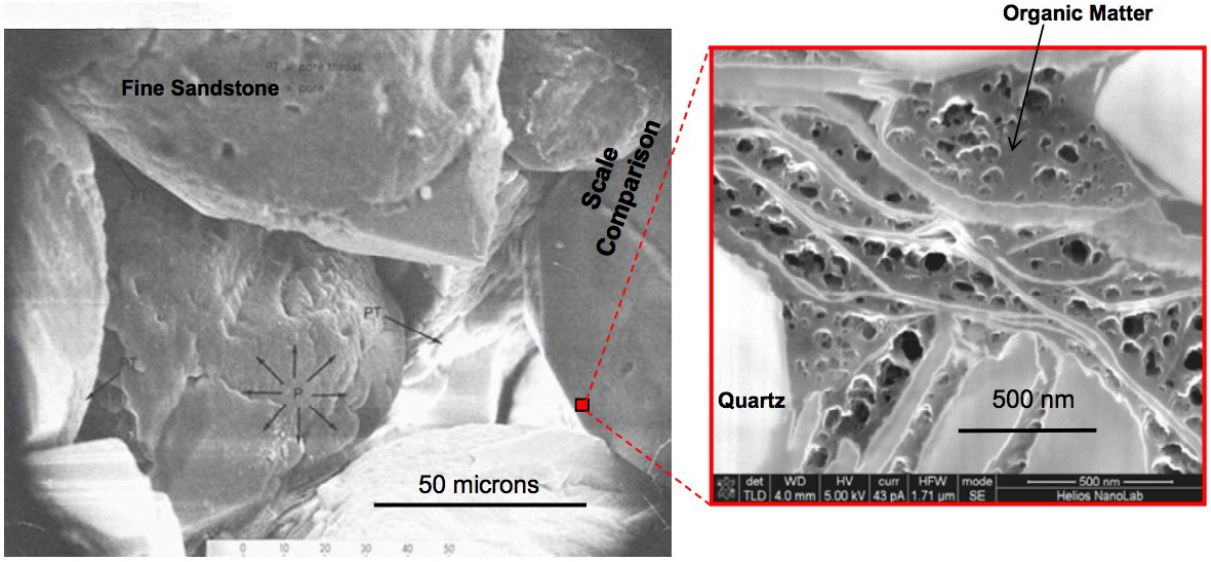

Figure 1 (Passey et. al. 2010): SEM photomicrograph of a fine-grained sandstone (left), and comparison of scale with porosity observed in organic matter in a Barnett organic-rich shale rock (right). The scale bar for the sandstone is 50 microns and for the organic matter inset image the scale bar is 500 nanometers.

1.1.3 Production of Shale Gas Reservoirs

Significant progress has been made in producing natural gas from unconventional reservoirs such as shales and tight gas formations in recent years. However, the estimated gas recovery from these reservoirs is still very low, estimated at 10 to 30 % of the gas in place. Gas flow in shale gas reservoirs is very complicated due to many coupled processes, such as gas adsorption/desorption, non-Darcy flow, strong rock/fluid interactions, a large Klinkenberg effect (Klinkenberg, 1941), and geomechanical effects. In addition, these processes coexist with complex flow geometry and multiscaled heterogeneity. The complicated flow behaviour impacts production and ultimate gas recovery in ways that are currently not well understood (Yu et al. 2014). The adsorbed gas is mostly produced in the latter stages of production when a considerable amount of free gas has been depleted and the well undergoes boundary dominated flow (Mengal and Wattenbarger, 2011). In early stage of production, when the pressure is high, the contribution from adsorbed gas to overall gas recovery is therefore usually insignificant (Yu and Sepehrnoori, 2014).

By combining horizontal drilling with hydraulic fracturing, a large and highly fractured network can be created in shale formations. Horizontal wellbores are drilled in the direction of minimum stress and multiple transverse hydraulic fractures are created in an attempt to maximize the total stimulated reservoir volume (Yu and Sepehrnoori, 2014). **Figure 2** shows an illustration of these two processes. The hydraulic fracturing process commonly uses a slurry of surfactants, corrosives, and aggregates to induce and maintain the fractures. After the stimulation pressure has been relieved, the aggregates are pinned by closure stresses and “prop” the fractures open,

which is why they are commonly referred to as proppants (Hellmann et al. 2014). Sustaining high fracture conductivity in propped hydraulic fractures is an important aspect of production in shale gas reservoirs. This can be challenging because of several effects that lead to reduced fracture conductivity such as proppant fines generation and migration (Pope et al. 2009), proppant diagenesis (LaFollette and Carman, 2010) also termed proppant scaling, proppant embedment in softer rock and proppant crushing in harder rock (Fan et al. 2010). Geomechanical effects, in the form of stress-dependence in hydraulic fractures, can also result in reduced permeability. All these effects increase with production as the drawdown pressure is decreased and may result in significantly lowered overall gas recovery in many shale gas reservoirs (Yu and Sepehrnoori, 2014).

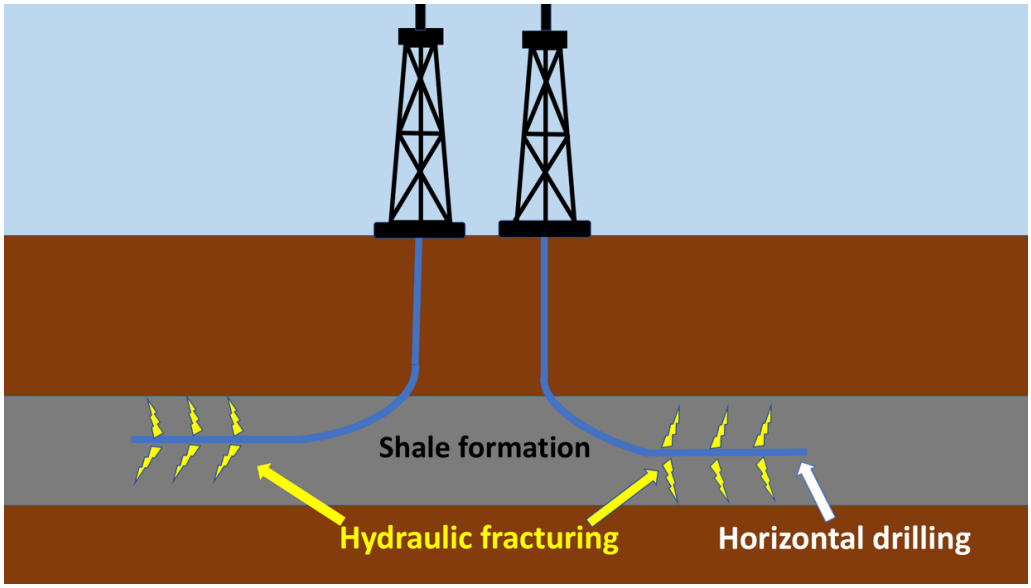

Figure 2: Illustration of horizontal drilling into a shale gas reservoir accompanied by hydraulic fracturing to maximize the total stimulated reservoir volume.

1.1.4 Modelling of Shale Gas Reservoirs

When it comes to predicting and evaluating well performance of shale gas reservoirs, reservoir modelling is the preferred method (Yu and Sepehrnoori, 2014). Shale gas reservoirs are difficult to accurately model because of features such as complicated flow regimes, gas adsorption and desorption, surface diffusion, and stress dependence which all affect the gas-flow- and production processes. When traditional models and simulators designed for conventional reservoirs are used to predict the gas originally in place (GOIP) of shale gas reservoirs, the volume occupied by the adsorbed gas is usually overlooked, and as a result the volume of free gas is significantly overestimated (Wang et al. 2017). Although there are a few shale gas reservoir simulators available, they do not comprehensively involve all of these important mechanisms (Cipolla et al. 2010; Kelkar and Atiq 2010; Yang et al. 2013; Guo et al. 2014; Wu et al. 2014). Very few studies have been carried out addressing the critical issues of how to accurately model fractured unconventional gas reservoirs and how to select the best approach for modelling a given shale gas formation. Model development is therefore an area that needs to be given more attention in order to improve this understanding. This can be achieved through coming up with new conceptual models and in-depth modelling studies of laboratory to field-scale applications (Yu et al. 2014).

1.2 Geomechanics in the Petroleum Industry

Geomechanics is the study of how soils and rocks deform, sometimes to failure, in response to changes of stress, pressure, temperature and other environmental parameters. Although geomechanics and its application to the petroleum industry was mostly ignored in earlier times, it has gained increasing interest over the last 30 years. It can be applied across all scales and to almost all aspects of petroleum extraction, from exploration to production and abandonment. Reservoir stimulation in the form of hydraulic fracturing was one of the first applications in the oil field to use geomechanics methods and is still a major development area. At the reservoir scale, geomechanics can help to model fluid movement and predict how fluid injection or removal effects the reservoir performance by changing important parameters like permeability, fluid pressure and in-situ rock stresses. In this way, geomechanics can be applied to make life-of-reservoir decisions such as placing and completing of new wells, enhancing and sustaining production, minimizing risk and making new investments. A major area where consideration of geomechanics effects is needed is in oil and gas production from shales, because mechanical anisotropy – the variation of mechanical properties with orientation – plays a vital role (Cook, 2015).

1.3 Scope of Project

A simplistic numerical modelling approach of a 1D+1D combined fracture-matrix model that characterizes fracture-matrix interactions is presented. The model is an extension of the work by Berawala et al. (2018), which was a continuation of other previous works such as Berawala et al. (2017**)** and Andersen et al. (2014, 2015). The new contributions to the previously constructed model is the incorporation of geomechanical effects and new scaling of dimensionless numbers, which was needed as a result of this incorporation. This means that the stress-dependence of porosity and permeability, which was previously ignored, has been taken into account. The model consists of a high-permeability fracture with length L_y extending out from a well perforation which is surrounded symmetrically on both sides by low-permeability shale matrix with length L_x. The width of the fracture is defined as $2b(y)$ and can vary as a function of distance from the well which depicts a real-field scenario. The system is solved numerically using an operator splitting approach, see **Appendix B)**. The new model aims to address the following questions: (i) How do geomechanical effects impact gas recovery in shale gas reservoirs? (ii) How is pressure, porosity and permeability affected by geomechanical effects? (iii) How do reservoir characteristics like fracture size, fracture shape, fracture spacing, and initial reservoir pressure affect gas recovery when geomechanical effects are included, and (iv) which geomechanical effects are most significant? These questions are answered by analysing the model behaviour in terms of gas recovery, parameterized using literature data and by analysing 2D plots of pressure, porosity and permeability distributions in the reservoir. A sensitivity analysis is performed to investigate the significance of different geomechanical effects when reservoir conditions are varied, and the results are interpreted. Finally, the model behaviour is interpreted using the dimensionless number derived from the new scaling approach.

1.4 Outline of Thesis

The rest of the thesis is as follows: All of chapter 2 consists of literature review and is divided into three subchapters. Subchapter 2.1 reviews the different mechanisms taking place in shale gas reservoirs which make the gas flow in these reservoirs difficult to accurately model. Subchapter 2.2 presents geomechanical effects in shale gas reservoir reported in the literature. Subchapter 2.3 presents different approaches to modelling geomechanical effects in shale gas reservoirs. The approach for incorporating geomechanics used in this model is presented in here. Chapter 3 describes the mathematical model. The 1D+1D mathematical model is derived from basic laws well known in the petroleum literature. The equations used for incorporating geomechanical effects and the incorporation into the model is summarized. It is shown how the new model is scaled to derive new dimensionless numbers α and β which characterize the system. In chapter 4 the simulation results obtained from the model are presented and observations are described. In chapter 5 the results are discussed, and the behaviour of the model is interpreted using dimensionless numbers.

2. Literature Review

2.1 Mechanisms in Shale Gas Reservoirs

Darcy's law (Darcy, 1856) for single phase gas flow is given by:

$$Q = \frac{KA}{\mu_g}\frac{\Delta P}{L} \quad (1)$$

where Q is the volumetric flow rate, A is the cross-sectional area, K is the permeability of the porous media, μ_g is the gas viscosity, ΔP is the pressure drop across the porous media and L is the length of the porous media. For one-directional flow (say, parallel to the x-axis), the equation can be written in the following differential form:

$$v = \frac{Q}{A} = -\frac{K}{\mu_g}\frac{\partial P}{\partial x} \quad (2)$$

where v is a superficial flow velocity and $\partial P/\partial x$ is the pressure gradient in the x-direction. The negative sign in (2) indicates that the pressure drop is in the direction of flow (Peaceman, 1977). Darcy's law is typically used to describe gas flow in conventional reservoirs. However, comprehensive reviews of the flow mechanisms in shale gas reservoirs suggest that the gas flow may not be accurately described using the traditional Darcy's law (Blasingame, 2008; Moradis et al. 2010). Mechanisms such as gas slippage (Klinkenberg effect) and Knudsen diffusion can result in non-Darcy flow behaviour in the reservoir by affecting the apparent gas permeability (Wang and Marongiu-Porcu, 2015). Other mechanisms will also impact the gas flow such as gas adsorption and desorption, surface diffusion, and geomechanical effects (Wu et al. 2014). A review of these important flow mechanisms in shale gas reservoirs are given in the following subchapters.

2.1.1 The Klinkenberg or Gas-Slippage Effect

In conventional reservoirs, where Darcy's law is used to model pressure-driven viscous flow, the fluid velocity at the pore walls is assumed to be zero. This is a good assumption in pores where the radius is in the range of 1 to 100 micrometres, because fluids flow as a continuous medium (Wang and Marongiu-Porcu, 2015). However, in shale gas reservoirs there are many nanosized pores where gas molecules strike against the pore walls and tend to slip instead of having zero velocity (Sherman, 1969). The gas-slippage effect, also referred to as the Klinkenberg effect, was first identified by Klinkenberg (1941) when he was studying rarefied gas flowing at various pressures. Through observation he discovered that the actual gas flow rate was consistently larger than the gas flow rate predicted with Darcy's law. To correct this error, he suggested that the apparent permeability be adjusted by a slippage factor (Wang and Marongiu-Porcu, 2015). If existing, the Klinkenberg effect will increase the gas permeability and productivity in a shale formation. Wang and Reed (2009) showed that the gas permeability in Marcellus shale increased from 19.6 microdarcies at 1000 psi to 54 microdarcies at 80 psi because of the strong Klinkenberg effect. Although this effect is maximized in low-pressure regions, it is expected to be significant in shale gas reservoirs even under high-pressure conditions (Wu et al. 2014). In order to incorporate the Klinkenberg effect into reservoir models the absolute permeability of gas can be modified as a function of gas pressure (e.g., Wu et al. 1998):

$$k_g = k_\infty\left(1 + \frac{b}{P_g}\right) \quad (3)$$

Where k_∞ is constant, absolute gas permeability under very large pressure (in which the Klinkenberg effect is minimized), and b is the Klinkenberg beta factor. The beta factor can be determined from laboratory as either a constant or as a pressure-dependent function. A table-lookup approach can also be applied to account for the Klinkenberg effect, where the apparent gas permeability is treated as a function of pressure (Wu et al. 2014).

2.1.2 Knudsen diffusion

In the nanopore structures of shale gas reservoirs there can exist flow regimes other than the well-understood continuum regime, such as slip-, transition-, and free molecular flow regimes. Knudsen diffusion is a type of diffusion that occurs when the gas molecules collide with the pore walls more frequently than with each other. The Knudsen number is a dimensionless parameter than can measure the degree of Knudsen diffusion and be used to differentiate between flow regimes in conduits at micro- and nanoscale (Wang and Marongiu-Porcu, 2015). The Knudsen number is defined as the ratio of the molecular mean free path length, λ, and the characteristic length of the channel, which in the case of shale gas reservoirs is the effective pore radius, r (Knudsen, 1909):

$$K_n = \frac{\lambda}{r} \tag{4}$$

The mean free path can be calculated from the relation in Civan et al. (2011):

$$\lambda = \frac{\mu_g}{P}\sqrt{\frac{\pi RT}{2M}} \tag{5}$$

where μ_g is the gas viscosity, T is the reservoir temperature, P is the reservoir pressure, M is the gas average molecular weight, and R is the universal gas constant. By including the real-gas Z-factor, one can substitute the mean free path into (4), which gives:

$$K_n = \frac{\mu_g Z}{Pr}\sqrt{\frac{\pi RT}{2M}} \tag{6}$$

Feil! Fant ikke referansekilden. shows how Knudsen number ranges are used to classify the different flow regimes that can occur in shale gas reservoirs. The Knudsen number in most shale gas reservoirs lies between 10^{-3} and 1, which means that the most likely flow regimes are the slip- and transition flow regimes (Ziarani and Aguilera, 2011). In order to incorporate Knudsen diffusion into reservoir models, the apparent permeability can be represented in the following general way:

$$k_a = k_\infty f(K_n) \tag{7}$$

where k_∞ is the intrinsic permeability of the porous medium, which is defined as the permeability for a viscous, nonreacting ideal liquid, and $f(K_n)$ is the correlation term that relates the matrix apparent permeability and intrinsic permeability (Wang and Marongiu-Porcu, 2015). Different models have been developed that quantify the relationship between intrinsic permeability and the nanopore structure in porous media (Beskok and Karniadakis, 1999; Aguilera 2002). Using the relation presented in Beskok and Karniadakis (1999), the intrinsic permeability can be derived from:

$$k_\infty = \frac{r^2}{8} \tag{8}$$

where r is the radius of a capillary tube which means that k_∞ is only related to the nanopore geometry. The correlation terms that relates the intrinsic and apparent permeability can be

derived from laboratory experiments (Wang and Marongiu-Porcu, 2015). Sakhaee-Pour and Bryant (2012) proposed a first-order permeability model in the slip regime:

$$f(K_n) = 1 + 5K_n \tag{9}$$

accompanied by a polynomial permeability model in the transition regime:

$$f(K_n) = 0.8453 + 5.4576K_n + 0.1633K_n^2 \tag{10}$$

Table 1 (Roy et al. 2003): How fluid flow regimes can be defined by ranges of the Knudsen number, K_n.

K_n	$0 - 10^{-3}$	$10^{-3} - 10^{-1}$	$10^{-1} - 10^{1}$	$> 10^{1}$
Flow Regime	Continuum	Slip	Transition	Free Molecular

2.1.3 Gas Adsorption and Desorption

There are mainly two isotherms used for modelling gas adsorption and desorption in shale gas reservoirs. Although recent investigations have observed that some shales obey the BET isotherm (Zhang and Yang 2012; Alnoaimi and Kovscek 2013; Yu et al. 2014), the Langmuir isotherm is in most publications to date to describe gas adsorption in shale gas reservoirs (Lu et al. 1995; Mengal and Wattenbarger 2011; Shabro et al. 2011; Dong et al. 2012; Haghshenas et al. 2013). The BET (Brunauer et al. 1938) isotherm is used to describe multilayer adsorption, while the Langmuir isotherm (Langmuir, 1918) indicates that the gas molecules obey monolayer adsorption. Accurate modelling of the adsorption isotherm is crucial for shale gas reservoir development because different isotherms represent different gas adsorption capacities and desorption processes which affect the gas production (Wang et al. 2017). When the Langmuir isotherm is applied, the amount of adsorbed gas on a solid surface is given by the Langmuir equation which characterizes the desorption process as a function of pressure at constant temperature:

$$G_s = \left(\frac{V_L P_g}{P_g + P_L}\right) \tag{11}$$

where G_s is the gas content, V_L is the Langmuir volume which represents the maximum storage capacity volume of gas, P_L is the Langmuir pressure and P_g is the pressure in the formation. As gas is produced through production wells in the reservoir, pressure decreases, and more adsorbed gas is released from the solid to the free gas phase in the pressure-lowering region. The Langmuir volume is a function of TOC and thermal maturity of the shale. The Langmuir pressure is defined as the pressure at which 50% of the gas is desorbed. The Langmuir modelling approach is based on the assumption that there exists an instantaneous equilibrium between pressure changes and the amount of adsorbed gas. This means that there is no transient-time lag between changes in pressure and the corresponding adsorption and desorption responses (Yu et al. 2014). Gao et al. (1994) reported that this instantaneous equilibrium assumption is reasonable because of the ultra-low permeabilities in shales which leads to very low flow rate through the kerogenic media within shales. The Langmuir isotherm is often determined in laboratory by using core samples (Yu and Sepehrnoori, 2014).

2.1.4 Surface Diffusion

Some experts have reported that the adsorbed gas layer in the organic matter is capable of transport in the form of surface diffusion under the gradient of concentration or chemical potential (Fathi and Akkutlu, 2013; Wu et al. 2015). However, there are conflicting arguments

in the literature concerning the adsorbed gas transport (Wasaki and Akkutlu 2014). Xiong et al. (2012) reported that surface diffusion will be dependent on the value of surface diffusivity, which is not well known and probably more important at low pressure in pores smaller than 5 nanometers. Similarly, Sigal (2013) proposed that adsorbed-layer diffusional transport requires large values of the diffusion constant and may then only be a second mechanism for the gas transport. Fathi and Akkutlu (2013) modelled surface diffusion after the lattice Boltzmann method which indicates that the adsorbed gas can be mobile under reservoir conditions. Some researchers also simply treat the adsorbed phase as immobile (Cui et la. 2009; Sakhaee-Pour and Bryant 2012).

2.1.5 Geomechanical Effects

The effect that geomechanics have on oil and gas production in conventional reservoirs is generally small. It has therefore been widely overlooked in practice. However, in unconventional shale gas reservoirs these effects can be relatively large due to nanosized pores and microfractures, and have to be considered, in general (Wu et al. 2014). Studies have shown that the permeability in shales is pressure dependent and decreases when the effective stress, or confining pressure is increased (Soeder, 1988; Bustin et al. 2008; Wang and Reed, 2009). The effect from confining pressure on permeability is caused by a reduction in porosity. The degree of permeability reduction taking place with increased confining pressure in shales is reportedly much higher than in consolidated sandstones or carbonates (Wu et al. 2014). The stress-dependence of hydraulic fractures in shale gas reservoir have been discussed in the literature, whilst the stress-dependence of matrix pores and natural fractures have been mostly ignored. However, these effects will affect the gas flow regimes in the reservoir by changing the pores sizes and should be taken into account (Wang et al. 2017).

2.2 Geomechanical Effects in Shale Gas Reservoirs

Wu et al. (2014) presented model-application examples illustrating the effect that stress-dependent matrix permeability had on gas production for a horizontal well with a 10-stage hydraulic fracture-system in an extremely tight, uniformly porous and/or fractured reservoir. When they investigated the effect of stress-dependent matrix permeability, a table-lookup approach was implemented where input data from **Figure 3** was used to describe the relationship between effective stress and matrix permeability. The figure shows how the gas permeabilities in different shales decrease when the effective stress, or confining pressure, is increased.

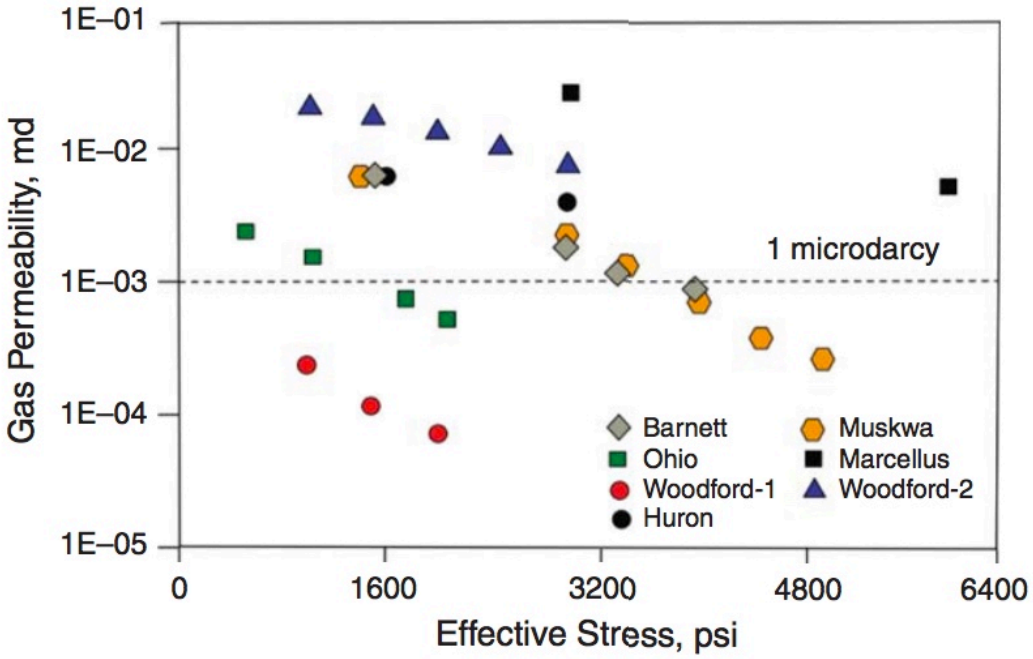

Figure 3 (Soeder, 1988; Wang and Reed, 2009): Effect of confining pressure, or effective stress, on gas permeability in different shales. The gas permeability in Muskwa shale is most sensitive to changes in effective stress, decreasing to around 1/20 of its original value when the effective stress is increased from 1600 psi to 4800 psi.

The effect from geomechanics on cumulative gas production was illustrated by Wu et al. (2014), as shown in **Figure 4**. It was observed that the geomechanics effect has a large impact on cumulative gas production and the impact increases with time. This impact on gas production comes from the reduction in formation permeability that occurs when the pore pressure declines and the confining pressure, or effective stress, is increased (Wu et al. 2014).

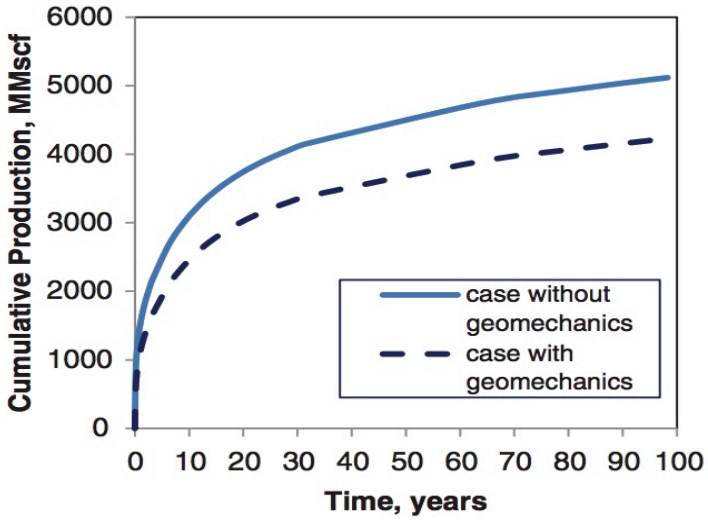

Figure 4 (Wu et al. 2014): Cumulative gas production vs. time with and without geomechanics. Geomechanical effects are shown to have a large impact on cumulative gas production and the impact increases with time.

The effect of stress-dependent matrix permeability on gas production was also investigated by Wang et al. (2017). They studied the effect on the Barnett shale, Marcellus shale no. 1 and Marcellus shale no. 2. **Figure 5** is taken from Wang et al. (2017) and shows the impact the

matrix permeability-stress-dependence factor, Ψ, has on gas production. One can observe that the cumulative gas production is decreased as the matrix permeability-stress-dependence factor is increased for all three shales. Noticeably, the reduction is largest for the Marcellus shale no. 1 which is explained by the fact that the density of fractures in Marcellus shale no. 1 is the lowest. This means that for Marcellus shale no. 1 matrix permeability is more essential for production and the reduction of matrix permeability has a more significant impact on gas production (Wang et al. 2017).

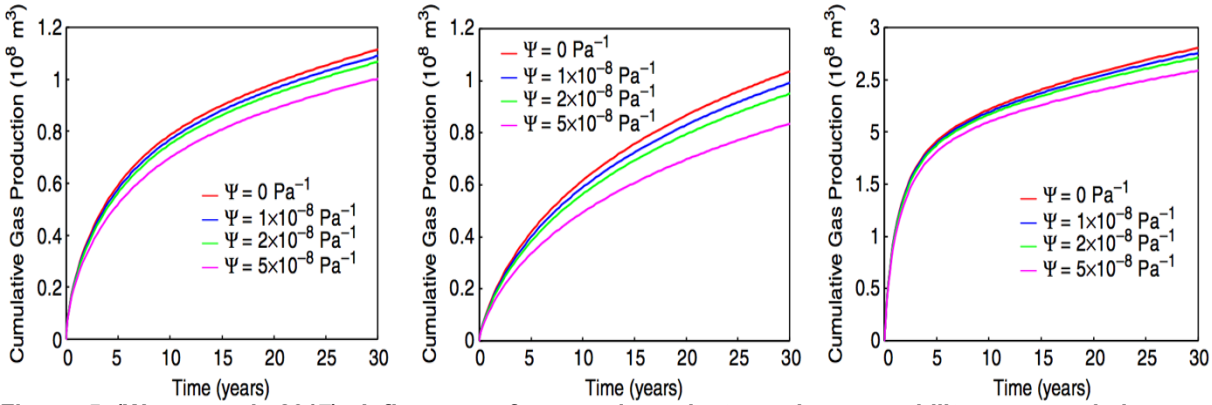

Figure 5 (Wang et al. 2017): Influences of stress-dependent matrix permeability on cumulative gas production for the Barnett shale (left), Marcellus shale no. 1 (middle) and Marcellus shale no. 2 (right). The effect is largest for Marcellus shale no. 1 because the density of fractures in the Marcellus shale no. 1 is lowest (fracture spacing is largest).

Yu and Sepehrnoori (2014) studied the effect that stress-dependent hydraulic fractures have on gas production. CMG modelling was used to model gas flow in two shale gas reservoirs. One of these reservoirs was in Barnett shale while the other was in Marcellus shale. To account for the stress-dependence of the hydraulic fractures a specific compaction table was integrated into the CMG simulator. They reported that after 4.5 years of production there was a 4.8% decrease in total gas production for the Barnett shale, and after 30 years of production the decrease was 1.8% for the Barnett shale and 23.3% for the Marcellus shale. Stress-dependent hydraulic fractures were seen to have a larger effect during early times of production than for late times of production and the effect was largest for the Marcellus shale. The Barnett- and Marcellus shale in the study were categorized as stiff and medium shales, respectively, according to their static Young's modulus. Yu and Sepehrnoori (2014) concluded, based on these results, that in formations with low Young's modulus the stress-dependence of hydraulic fractures plays a significant role on gas production and should be considered in modelling of shale gas reservoirs. Additionally, they concluded that in formations with high Young's modulus the stress-dependence of hydraulic fractures might be ignored when modelling shale gas reservoirs.

2.3 Modelling Geomechanics in Shale Gas Reservoirs

2.3.1 Stress-Dependent Matrix

In the approach proposed by Yu et al. (2014), the effective porosity and permeability of rock are also assumed to correlate with the mean effective stress (σ'_m), defined as:

$$\sigma'_m = \sigma_m(x, y, z, P) - \alpha P \quad (12)$$

where α is the Biot constant and the initial distribution of effective stress is:

(13) $$\sigma_m(x,y,z,P) = \frac{\sigma_x(x,y,z,P) + \sigma_y(x,y,z,P) + \sigma_z(x,y,z,P)}{3}$$

where σ_x, σ_y, and σ_z are total stress in the x-, y-, and z-direction, respectively. The effective porosity and intrinsic permeability of rock are then assumed to correlate with the mean effective stress only:

(14) $$\phi = \phi(\sigma'_m)$$
$$K = K(\sigma'_m)$$

There are many correlations that have been used to represent the relation between matrix porosity and effective stress (Davies and Davies, 1999; Rutqvist et al. 2002; Winterfeld and Wu, 2011). The most commonly used correlation is the one presented by Rutqvist et al. (2002):

(15) $$\phi^m(P_g) = \phi_r + (\phi_0 - \phi_r)e^{-\eta_m \sigma'_m}$$

This means that the initial matrix porosity can be given by:

(16) $$\phi_i^m = \phi_r + (\phi_0 - \phi_r)e^{-\eta_m \sigma'_{m,i}}$$

where $\phi(P_g)$ is the porosity considering stress sensitivity, ϕ_r is the high-effective-stress porosity, ϕ_0 is the porosity at effective mean stress $\sigma_m = 0$, ϕ_i^m is the matrix porosity at initial reservoir conditions, η_m is the matrix porosity-stress-dependence factor in Pa^{-1} and σ_m is the mean effective stress in Pa. Rutqvist et al. (2002) also presented an associated function for permeability in terms of porosity:

(17) $$K = K_0 e^{c\left(\frac{\phi}{\phi_0} - 1\right)}$$

where c is a parameter. The applicability of this approach requires that the initial distribution of effective stress is predetermined as a function of spatial coordinates and pressure fields, as in (13). Since the changes in effective stress are mainly caused by changes in reservoir pressure, the stress distribution can be estimated analytically, numerically, or from field measurements. The approach can be significantly simplified by assuming that the in-situ total stress in the reservoir as nearly constant, or a function of spatial coordinates and fluid pressure only during production (Yu et al. 2014). Another closely related approach to incorporating stress-dependent matrix pores was presented by Wang et al. (2017). The mean effective stress in this approach is mainly related to the vertical overburden load and reservoir pressure (Raghavan and Chin, 2004):

(18) $$\sigma'_m = \sigma_{m,tot}(\sigma_{ob,v}) - P_g$$

Similarly, the initial mean effective stress can be expressed as:

(19) $$\sigma'_{m,i} = \sigma_{m,tot}(\sigma_{ob,v}) - P_{init}$$

where $\sigma_{m,tot}$ is the total mean stress pressure and $\sigma_{ob,v}$ is the vertical overburden load. This approach assumes that the total mean stress pressure, $\sigma_{m,tot}$, is a function of $\sigma_{ob,v}$ and is nearly a constant value for the system studied. The approach also assumes that the effective porosity and permeability of rock correlate with the mean effective stress only, as in (14)(14), and that the stress-dependent porosity can be expressed by (15)(15). By substituting (18) and (19) into (15)(15) and (16)(16) for σ_m and $\sigma_{m,i}$, respectively, we obtain the matrix porosity as a function of reservoir pressure:

(20) $$\phi(P_g) = \phi_r + (\phi_i^m - \phi_r)e^{-\eta_m(P_{init} - P_g)}$$

Instead of using (17) as the expression of stress-dependent permeability, the function presented by Raghavan and Chin (2004) can be used:

$$K^m(P_g) = K_0^m e^{-\Psi_m \sigma'_m} \quad (21)$$

where K_0^m is the matrix permeability at effective mean stress $\sigma'_m = 0$ and Ψ_m is the permeability-stress-dependence factor for the matrix in Pa^{-1}. This correlation is in good agreement with experimental data in studies on gas permeability in shales by Soeder (1988), Bustin et al. (2008), and Wang and Reed (2009). Similarly, the initial permeability of the matrix is then given by:

$$K_i^m = K_0^m e^{-\Psi_m \sigma'_{m,i}} \quad (22)$$

Treating (21) and (22) as we treated (15) and (16), by substituting in (18) and (19) for σ'_m and $\sigma'_{m,i}$, respectively, we obtain the absolute permeability of the matrix pores as a function of reservoir pressure:

$$K^m(P_g) = K_i^m e^{-\Psi_m (P_{init} - P_g)} \quad (23)$$

An alternative way of incorporating the stress-dependence of matrix pores is to use a table-lookup approach for the correlations of porosity and permeability as functions of mean effective stress. The functions will then have to be determined from laboratory studies for a given shale gas reservoir (Yu et al. 2014).

2.3.2 Stress-Dependent Hydraulic Fractures

The conductivities of both propped and unpropped hydraulic fractures have been shown in experimental results to decrease with the increase of closure stress (Franquet et al. 2011; Alrahami and Sundberg, 2012; Kamenov et al. 2013; Warpinski et al. 2013). The closure stress, or confining pressure, is referred to as the difference between the minimum horizontal stress and the pore pressure in the fracture. The fracture conductivity can be defined in reservoir modelling as the product of fracture width and permeability:

$$F_c = w_f K_f \quad (24)$$

where F_c is fracture conductivity, w_f is fracture width, and K_f is fracture permeability (Yu and Sepehrnoori, 2014). Wang et al. (2017) incorporated stress-dependent fracture permeability into their modelling to account for the reduction in hydraulic fracture conductivity. According to experimental results (Kamenov et al. 2013; Yu and Sepehrnoori 2013), the relationship between effective permeability and reservoir pressure in hydraulic fractures can be expressed by:

$$K^f(P_g) = K_0^f e^{-\Psi_f \sigma'_m} \quad (25)$$

where K_0 is the fracture permeability at effective mean stress $\sigma_m = 0$, Ψ_f is the permeability-stress-dependence factor for the hydraulic fracture in Pa^{-1} and $K^f(P_g)$ is the permeability of the hydraulic fracture considering the stress-dependence effect. Similarly, the initial permeability of the hydraulic fracture can be given by:

$$K_i^f = K_0^f e^{-\Psi_f \sigma'_{m,i}} \quad (26)$$

By again handling (25) and (26) as (15) and (16) was handled earlier, we can express the permeability in the hydraulic fracture as a function of reservoir pressure:

$$K^f(P_g) = K_i^f e^{-\Psi_f (P_{init} - P_g)} \quad (27)$$

Another way of capturing the stress-dependent hydraulic fracture conductivity is to integrate a specific compaction table into the simulator. The compaction table feature can be assigned to cells describing hydraulic fractures and account for the reduction in fracture conductivity as the closure stress is increased during production. **Figure 6** shows laboratory data published by Alrahami and Sundberg (2012) describing the effect that closure stress has on the propped hydraulic fracture conductivity in stiff, medium and soft shales. These data can be applied to

account for reduced fracture conductivity in different shales. Large reductions in fracture conductivity is associated with soft shales that have a low static Young's modulus. Table ?? shows how shales can be categorized as stiff, medium, or soft depending on the value of their static Young`s modulus.

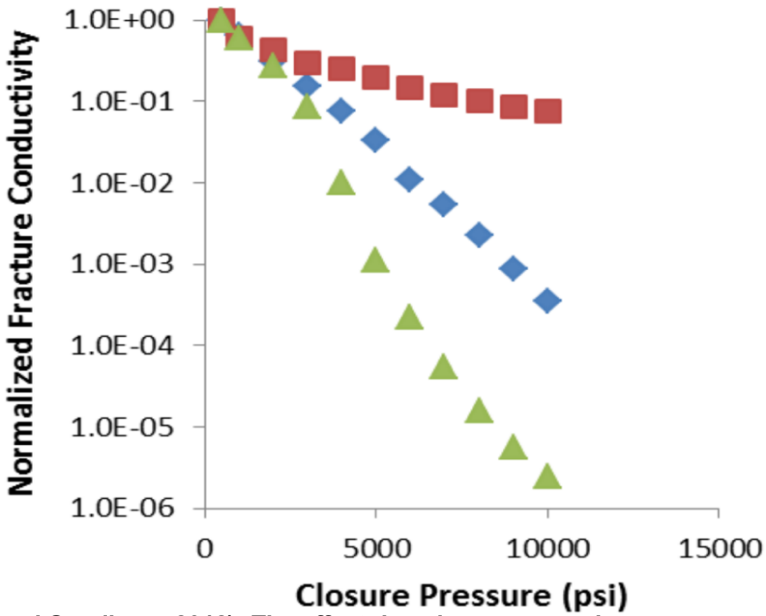

Figure 6 (Alramahi and Sundberg, 2012): The effect that closure stress has on propped hydraulic fracture conductivity in shales categorized as stiff, medium and soft. The data are normalized to the fracture conductivity measured at a closure pressure of 3.45 MPa.

Table 2 (Yu and Sepehrnoori, 2014): How shales are categorized as stiff, medium, or soft depending on the value of their static Young's modulus.

Shale Type	Young's Modulus (Pa)
Stiff	3.45e+10 – 6.9e+10
Medium	1.38e+10 – 3.45e+10
Soft	> 1.38e+10

3. Mathematical Model

The derivation of this model follows the derivation presented in Berawala et al. (2018). The contribution to this extended model is the incorporation of geomechanical effects on the formation of the shale gas reservoir. These effects are included by treating matrix and fracture properties that were previously considered as constant, as stress-dependent properties.

3.1 Assumptions

A simplified model is proposed that can represent important aspects of shale gas production. The main assumptions on the fracture and matrix domains are:

- A single hydraulic fracture of length L_y drains gas from symmetrically surrounding shale matrix of length $\mathrm{L_x}$.
- Variable fracture width $2b(y)$ is considered as a function of distance y from the well.
- The matrix symmetrically surrounds the fracture and the system is repetitive (has equally spaced fractures) so that there is a no-flow boundary at $\mathrm{x = L_x}$ (the matrix half-length).
- Pressure driven diffusion flow is the main driving force for gas flow from the matrix to the fracture and from fracture to the well.
- In the matrix gas only flows in the direction perpendicular to the fracture (the x-direction) and in the fracture gas only flow in the direction of the fracture (the y-direction).
- Single-phase flow of gas is considered so it is assumed that the reservoir is a dry gas or that it contains insignificant amount of water.
- Desorption of gas is pressure dependent which is defined by the Langmuir isotherm.
- The composition and flow properties of free and desorbed gas are the same.
- The gas is ideal and has constant viscosity μ_g.
- The model is considered to be horizontal with a constant height h.

3.2 Geometry

A hydraulic fracture extends perpendicularly out from a horizontally drilled well. The positive y-axis is defined along the fracture and pointing away from the well perforation. The length of the fracture is $\mathrm{L_y}$ and the fracture has a width, $\mathrm{2b(y)}$, which can vary with distance y from the well perforation. An illustration of the system geometry is given in **Figure 7**. The matrix surrounding the fracture is assumed to behave symmetrically. We obtain a no-flow boundary at $\mathrm{x = L_x}$ (the matrix half-length) by assuming that the given system is repetitive (has equally spaced fractures). We can therefore account for production from both sides by only solving the equations for one side of the system. In the following we only study the matrix located on the right side of the fracture ($\mathrm{0 < x < L_x}$). The fracture and matrix domains are given by:

$$\Omega^f = \{(x,y): -2b(y) < x < 0; 0 < y < L_y\}$$
$$\Omega^m = \{(x,y): -2b(y) - L_x < x < -2b(y);\ 0 < x < L_x; 0 < y < L_y\} \quad (28)$$

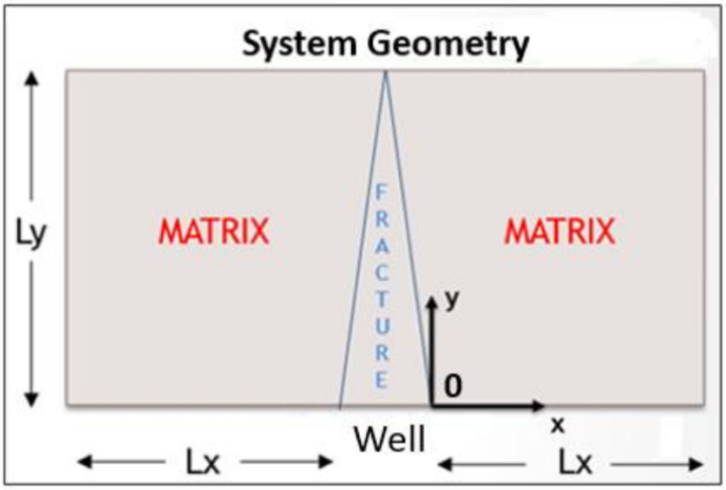

Figure 7 (Berawala et al. 2018): System geometry. A fracture with variable width extends from the well perforation with length L_y. The symmetrically surrounding shale matrix has a total length of $2L_x$.

3.3 Modelling Approach

3.3.1 Mass Conservation Equations

Consider that shale gas in free and adsorbed form is contained inside a domain Ω which has a volume V. Because of flow in and out of the interface $\delta\Omega$ with area A, the mass of gas in the porous media volume changes as expressed by the mass balance equation (LeVeque, 2002):

$$\frac{\partial}{\partial_t}\int_{\Omega}\left(\phi\rho_g + (1-\phi)a_g\right)dV = -\int_{\Omega}\left(\rho_g \boldsymbol{u}\right)\cdot \boldsymbol{n}dA \tag{29}$$

where ϕ is porosity, $\rho_g(P_g)$ is gas density, a_g is adsorbed gas (mass per solid volume), $\boldsymbol{u}$ is the Darcy mass flux vector, $\boldsymbol{n}$ is the unit normal vector pointing out of Ω, and P_g is the gas pressure.

Fracture domain

The gas adsorption in the fracture is considered negligible, thus $a_g^f = 0$. The fracture width, denoted $2b(y)$, can vary with the distance from the well. The fracture height, denoted h, is constant. Consider a volume $V = \int_y 2b(y)\,hdy$. From (29) we get:

$$\begin{aligned}\frac{\partial}{\partial_t}\int_{y-\frac{\Delta y}{2}}^{y+\frac{\Delta y}{2}}\phi\rho_g 2b(y)\,hdy \\ \approx \left(\rho_g u\right)_{y-\frac{\Delta y}{2}} 2b_{y-\frac{\Delta y}{2}} h - \left(\rho_g u\right)_{y+\frac{\Delta y}{2}} 2b_{y+\frac{\Delta y}{2}} h \\ + \left(\rho_g u\right)_{x=-2b,y}\Delta y h - \left(\rho_g u\right)_{x=0,y}\Delta y h\end{aligned} \tag{30}$$

When we divide (30) by $\Delta y h$ and let $\Delta y \rightarrow 0$, we get:

$$\partial_t\left(\phi\rho_g 2b\right) = -\partial_y\left(\rho_g u 2b\right) + \left(\rho_g u\right)_{x=-2b,y} - \left(\rho_g u\right)_{x=0,y} \tag{31}$$

Since the fracture is surrounded symmetrically by matrix on both sides the contribution from the two source terms is identical, i.e.:

$$\left(\rho_g u\right)_{x=-2b,y} = -\left(\rho_g u\right)_{x=0,y} \tag{32}$$

and we obtain:

$$\partial_t\left(\phi\rho_g b\right) = -\partial_y\left(\rho_g u b\right) - \left(\rho_g u\right)_{x=0,y} \tag{33}$$

Matrix domain

In the matrix it is assumed that the pressure gradient directs all flow in the x-direction (towards the fracture) and flow in the y-direction is ignored. Letting the volume be defined as $V = \Delta x \Delta y h$ and letting $(\rho_g u) \cdot j = 0$, where j is the unit vector in y-direction, we get from (29):

$$\frac{\partial}{\partial_t}\int_{x-\frac{\Delta x}{2}}^{x+\frac{\Delta x}{2}}\int_{y-\frac{\Delta y}{2}}^{y+\frac{\Delta y}{2}}\left(\phi\rho_g + (1-\phi)a_g\right)dxdyh = \left(\rho_g u\right)_{x-\frac{\Delta x}{2},y}\Delta yh - \left(\rho_g u\right)_{x+\frac{\Delta x}{2},y}\Delta yh \tag{34}$$

Dividing by $\Delta x \Delta y h$ and letting $\Delta x, \Delta y \rightarrow 0$ gives:

$$\partial_t\left(\phi\rho_g + (1-\phi)a_g\right) = -\partial_x(\rho_g u) \tag{35}$$

3.3.2 Darcy's law

The flux vector $\boldsymbol{u}$ is assumed to be related to pressure through Darcy's law (2):

$$\boldsymbol{u} = -\left(\frac{K}{\mu_g}\right)\nabla P_g \tag{36}$$

where the gas viscosity, μ_g, is considered independent of gas pressure and thus constant.

3.3.3 Density-Pressure Relations

The inverse gas volume factor, b_g, is introduced using the real gas law:

$$\rho_g(P_g) = b_g(P_g)\rho_{gs} \qquad b_g(P_g) = \frac{T^{atm}}{Z(P_g)TP_g^{atm}}P_g \tag{37}$$

Assuming that the gas is ideal ($Z = 1$) it is observed that:

$$\rho_g(P_g) = \rho_{gs} b_g' P_g \qquad b_g' = \frac{T^{atm}}{TP_g^{atm}} \tag{38}$$

where b_g' is the inverse volume factor differentiated with respect to pressure which is seen to be constant and has the unit of inverse pressure.

3.3.4 Shale Gas Adsorption

The conserved property $\phi\rho_g + (1-\phi)a_g$ can be expressed as:

$$\begin{aligned}\phi\rho_g + (1-\phi)a_g &= \phi\rho_{gs}b_g'P_g + (1-\phi)a_g \\ &= \phi\rho_{gs}b_g'\left(P_g + \left(\frac{(1-\phi)}{\phi\rho_{gs}b_g'}\right)a_g\right) = \phi\rho_{gs}b_g'\left(P_g + \hat{a}_g\right)\end{aligned} \tag{39}$$

where we have defined that:

$$\hat{a}_g = \left(\frac{1-\phi}{\phi\rho_{gs}b_g'}\right)a_g \tag{40}$$

The pressure dependency of $\hat{a}_g$ is related through the Langmuir adsorption relation (11):

$$\hat{a}_g(P_g) = \hat{a}_{max}\left(\frac{P_g}{P_g + P_L}\right) \tag{41}$$

where we have defined the gas content G_s as $\hat{a}_g(P_g)$, and the Langmuir volume V_L as:

$$\hat{a}_{max} = \left(\frac{(1-\phi)}{\phi\rho_g b_g'}\right)a_{max} \tag{42}$$

Note that $\hat{a}_g$, $\hat{a}_{max}$ and P_L all have the unit of pressure.

3.3.5 Stress-dependent Formation

For the incorporation of stress dependent formation, we first assume that the effective stress is mainly related to the vertical overburden load and reservoir pressure, as in (18) presented by Raghavan and Chin, 2004:

$$\sigma'_m = \sigma_{m,tot}(\sigma_{ob,v}) - P_g \tag{43}$$

Similarly, the initial mean effective stress can be expressed as in (19):

$$\sigma'_{m,i} = \sigma_{m,tot}(\sigma_{ob,v}) - P_{init} \tag{44}$$

where $\sigma_{m,tot}$ is the total mean stress pressure and $\sigma_{ob,v}$ is the vertical overburden load. This approach assumes that the total mean stress pressure, $\sigma_{m,tot}$, is a function of $\sigma_{ob,v}$ and is nearly a constant value for the system studied. The stress-dependence of porosity in the matrix is then incorporated through use of (43) and (44)(44), combined with (15) and (16), which gives:

$$\phi(P_g) = \phi_r + (\phi_i^m - \phi_r)e^{-\eta_m(P_{init}-P_g)} \tag{45}$$

Similarly, stress dependent matrix permeability is incorporated using (43) and (44)(44), combined with (21) and (22), which gives:

$$K(P_g) = K_0 e^{-\Psi_m(P_{init}-P_g)} \tag{46}$$

Finally, in the same manner, the stress dependent fracture permeability is incorporated using (43) and (44)(44), combined with (25) and (26), and we obtain:

$$K^f(P_g) = K_i^f e^{-\Psi_f(P_{init}-P_g)} \tag{47}$$

3.3.6 Initial and Boundary Conditions

At initial conditions ($t = 0$) the fracture and matrix have the same pressure, P_{init}. The adsorbed gas in the matrix is in equilibrium with this initial pressure:

$$P_g(t=0) = P_{init} \qquad \hat{a}_g(t=0) = \hat{a}_{max}\left(\frac{P_{init}}{P_{init}+P_L}\right) \tag{48}$$

The perforation is defined at $y = 0$ and has a known pressure, P_{well}:

$$P_g^f(y=0) = P_{well} \qquad (x \in \Omega^f) \tag{49}$$

There is pressure and mass flux continuity across the fracture-matrix boundary:

$$P_g\big|_{x=0^-} = P_g\big|_{x=0^+} \qquad (\rho_g u)_{x=0^-} = (\rho_g u)_{x=0^+} \tag{50}$$

The fracture is closed (or has negligible production) from the matrix in the y-direction. Similarly, the matrix has no flow at its outer boundary, due to symmetry:

$$\delta_y P_g\big|_{y=L_y} = 0 \qquad \delta_x P_g\big|_{y=L_x} = 0 \tag{51}$$

3.3.7 Summary of Model

By substituting (36)-(42) in (33) and (35) we can summarize the system for gas flow in the fracture-matrix system:

$$\partial_t(bP_g\phi^f) = \left(\frac{1}{\mu_g}\right)\partial_y(P_g b(y)K^f\delta_y P_g) + \left(\frac{K^m}{\mu_g}\right)(P_g\delta_x P_g)_{x=0,y} \qquad (x,y \in \Omega^f) \tag{52}$$

$$\partial_t\left(\phi^m(P_g + \hat{a}_g)\right) = \left(\frac{1}{\mu_g}\right)\partial_x(P_g K^m \partial_x P_g) \qquad (x,y \in \Omega^m) \tag{53}$$

(54) $$\hat{a}_g = \hat{a}_{max}\left(\frac{P_g}{P_g + P_L}\right)$$

These flow equations must be solved together with the initial and boundary conditions (48)-(51).

3.3.8 Scaling and Reduced 1D+1D Model

The system can now be scaled by introducing the following dimensionless variables:

(55) $$P' = \frac{P_{well} - P_g}{\Delta P} \qquad y' = \frac{y}{L_y} \qquad x' = \frac{x}{L_x} \qquad b' = \frac{b}{b_0}$$
$$D'(P') = \frac{P(P')}{P_{avr}} \qquad \hat{a}'_g = \frac{\hat{a}_g}{\Delta P}$$

(56) $$\phi' = \left(\frac{\phi}{\phi_{ref}}\right) \qquad K' = \left(\frac{K}{K_{ref}}\right)$$

where the pressure change and average pressure during production is defined as:

(57) $$\Delta P = P_{well} - P_{init} < 0 \qquad P_{avr} = \frac{1}{2}(P_{well} + P_{init})$$

and the reference porosity and permeability are defined as:

(58) $$\phi_{ref} = \left(\frac{1}{2}\right)\left(\phi(P_{init}) + \phi(P_{well})\right) \qquad (K_{ref}) = \left(\frac{2}{\left(\frac{1}{K(P_{init})}\right) + \left(\frac{1}{K(P_{well})}\right)}\right)$$

The average width of the fracture is $2b_0$ so that the relation to the area of the fracture is given by $2b_0 L_y = \int_{y=0}^{L_y} 2b(y)dy$. D' is scaled by the average pressure because it represents the part of the gas diffusion coefficient resulting from the absolute pressure. The scaled variables given in (55)(55) have coordinates that obey $0 \leq x', y' \leq 1$.The scaled pressure P' takes an initial value of 1 and decreases to 0 as the well pressure is reached. The scaled porosity and permeability values obtained from (56) combined with (58) are representative values that control the production rate and time scale. They will have coordinates that take initial values above 1 and final values below 1 when geomechanical effects are considered. To get the average scaled porosity and permeability the following formulas have been used:

(59) $$\phi'^{m}_{avg} = \frac{\sum_{i=1}^{n_y}\sum_{j=2}^{n_x}\phi'^{m}}{(n_x - 1)n_y} \qquad \phi'^{f}_{avg} = \frac{\sum_{i=1}^{n_y}\phi'^{f}}{n_y}$$

(60) $$K'^{m}_{avg} = \frac{(n_x - 1)n_y}{\sum_{i=1}^{n_y}\sum_{j=2}^{n_x}\left(\frac{1}{K'^{m}}\right)} \qquad K'^{f}_{avg} = \frac{n_y}{\sum_{i=1}^{n_y}\left(\frac{1}{K'^{f}}\right)}$$

By applying the previous equations (52) and (53) we can define two natural time scales: τ^f, representing the diffusion of gas from the fracture to the well, and τ^m, representing the diffusion of free gas and adsorbed gas from the matrix to the fracture. The time scales are given as follows:

(61) $$\tau^f = \left(\frac{\mu_g \phi^f_{ref} L_y^2}{K^f_{ref} P_{avr}}\right) \qquad \tau^m = \left(\frac{\mu_g (\partial_p G)_{ref} L_x^2}{P_{avr} K^m_{ref}}\right)$$

where:

(62) $$(\partial_p G)_{ref} = \frac{G(P_0) - G(P_{well})}{P_0 - P_{well}}$$

and:

(63) $$G = \phi^m\left(P_g + \hat{a}_{max}\left(\frac{P_g}{P_g + P_L}\right)\right)$$

In the following we scale time with respect to the fracture diffusion time scale:

$$t' = \frac{t}{\tau^f} \tag{64}$$

After scaling, the gas flow transport system given by (52) and (53) can be expressed in the following form:

$$b'\partial_{t'}(P'\phi'^f) = \partial_y\left(D'b'K'^f\partial_{y'}P'\right) + \alpha\beta\left(D'K'^m\partial_{x'}P'\right)_{x'=0,y'} \quad \left(x', y' \in \Omega^{\mathrm{f}}\right) \tag{65}$$

$$\partial_{t'}G' = \alpha\partial_x\left(D'K'^m\partial_x P'\right) \quad (x', y' \in \Omega^m) \tag{66}$$

All constant terms have been collected in two dimensionless numbers:

$$\alpha = \frac{\tau^f}{\tau^m} = \frac{K^m_{ref}\phi^f_{ref}L_y^2}{K^f_{ref}(\partial_P G)_{ref}L_x^2} \tag{67}$$

and:

$$\beta = \left(\frac{(\partial_P G)_{ref}L_x}{\phi^f_{ref}b_o}\right) \tag{68}$$

α represents the ratio of the time scales involved in gas diffusion from the fracture and gas diffusion from the matrix, including desorption, respectively. β denotes the capacity ration of the matrix relative to the fracture. Finally, the initial and boundary conditions in scaled terms become:

$$P'(t' = 0) = 1, \quad \hat{a}'_g(t' = 0) = \hat{a}'_{max}\frac{P_{init}}{P_{init}+P_L} \tag{69}$$

$$P'(y' = 0) = 0 \qquad \partial_{y'}P'\big|_{y'=1} = 0 \qquad \left(x', y' \in \Omega^{\mathrm{f}}\right) \tag{70}$$

$$\partial_{x'}P'\big|_{x'=1} = 0 \qquad (x', y' \in \Omega^{\mathrm{m}}) \tag{71}$$

4. Simulation Results

In this chapter the behaviour of the model will be investigated by considering its sensitivity to different input parameters. Since this model has introduced geomechanical effects into a previously existing model, the main focus of the investigation is on how geomechanical effects influence the matrix and fracture properties and gas recovery profiles. In order to investigate controlling parameters on gas recovery, other input parameters will also be varied concurrently with varying the geomechanical effects. An operator splitting approach is used for solving the system, similar to that described in Andersen et al. (2014, 2015), see **Appendix B**). This entails that we alternate between solving for flow in the y-direction (fracture diffusion) and in the x-direction (fracture-matrix diffusion and desorption). In order to switch sufficiently frequent between the two solvers, the operator spitting time step was selected at least 300 times lower than the time scale of fracture diffusion τ_f. The numerical solution procedure is described in detail in **Appendix C)**. The y-axis was discretised into 20 equal cells n_y and the (positive) x-axis was discretised into 30 equal cells n_x in addition to the fracture cell. In the following, the gas recovery factor RF is reported as the produced fraction of the mass initially in the reservoir:

$$RF = 1 - \frac{GCIP}{GOIP} = 1 - \frac{GCIP}{GOIP(P_{init})} \tag{72}$$

Additionally, the obtainable gas recovery factor RF_{ob} is reported, defined as the produced fraction of the mass that could be produced if the reservoir pressure was lowered uniformly from P_{init} to P_{well}:

$$RF_{ob} = \frac{RF}{RF_{\infty}} = \frac{GCIP(P_{init}) - GCIP}{GCIP(P_{init}) - GCIP(P_{well})} \tag{73}$$

where the recovery factor RF_{∞} is defined as the gas recovery when the reservoir pressure has been lowered uniformly from P_{init} to P_{well}:

$$RF_{\infty} = 1 - \frac{GCIP(P_{well})}{GOIP} = 1 - \frac{GCIP(P_{well})}{GOIP(P_{init})} \tag{74}$$

4.1 Model Input

The input parameters used in the simulation cases, unless otherwise is stated, are held constant and equal to the values listed in **Table 3**. The Langmuir isotherm parameters are representative of Marcellus shale and were taken from Yu et al. (2016). Almost all the remaining input parameter values are taken from Berawala et al. (2018). The only exception is the high-effective-stress porosity, ϕ_r, which is taken from Wang et al. (2017).

Table 3: Input parameters used in simulation cases ([1] Yu et al. 2016, [2] Berawala et al. 2018, [3] Wang et al. 2017).

Parameter	Value	Unit
[1] Initial reservoir pressure, P_{init}	344.7	bar
[2] Gas viscosity, μ_g	0.0184	cP
[2] Gas density at standard condition, ρ_{gs}	0.7	kg/Sm^3
[2] Initial matrix permeability, K_i^m	10	µD
[1] Initial matrix porosity, ϕ_i^m	0.15	-
[2] Matrix half-length, L_x	25	m
[2] Fracture half-length, L_y	7	m
[2] Max-to-min fracture width ratio, $\frac{b_{max}}{b_{min}}$	1	-
[2] Average fracture half-width, b_0	0.02	m
[2] Fracture porosity, ϕ^f	0.60	-
[2] Initial fracture permeability, K_i^f	10	mD
[2] Bottom hole well pressure, P_{well}	17.24	bar
[1] Langmuir max adsorption capacity, a_{max}	5.023	kg/m^3
[1] Langmuir half-capacity pressure, P_L	27.58	Pa
[1] Reservoir temperature, T	323.15	K
[3] High-effective-stress porosity, ϕ_r	0.05	-

Although the fracture in most simulation cases is assumed to have a constant width, we will also consider cases where the fracture shape varies. In these cases, the fracture width $b(y)$ will decrease linearly with distance y from the well and be defined by three parameters; the length L_y, the average half-width b_0, and the max-to-min width ratio $\frac{b_{max}}{b_{min}}$:

$$b(y) = 2b_0\left(\frac{\frac{b_{max}}{b_{min}}}{\left(\frac{b_{max}}{b_{min}}+1\right)} - \frac{\left(\frac{b_{max}}{b_{min}}-1\right)}{\left(\frac{b_{max}}{b_{min}}+1\right)}\left(\frac{y}{L_y}\right)\right) \tag{75}$$

where b_{max} is the fracture width at $y = L_y$ (end of fracture) and b_{min} is the fracture width at $y = 0$ (closest to the well) (see **Figure 7**). Three geomechanical parameters will determine the effects from geomechanics on the matrix porosity and matrix and fracture permeability; the matrix porosity-stress-dependence factor, η_m, the matrix permeability-stress-dependence factor, Ψ_m, and the fracture permeability-stress-dependence factor, Ψ_f. The values given to the geomechanical parameters will be varied during the sensitivity analysis and are specified at the start of every subchapter.

4.2 Previous Model Findings

In the previous model, from which this model is extended to include geomechanical effects, some of the following findings were made. For that model, Berawala et al. (2018) presented the scaled pressure distribution $P'(x', y')$ and mass fraction of adsorbed gas relative to total mass $\frac{\hat{a}(P_g)}{\hat{a}(P_g)+P_g}$ at different stages of recovery, as shown in **Figure 8**. They found that pressure declines quickly in the fracture at production start, followed by pressure decline in the surrounding matrix. This causes gas to desorb out of the kerogen into the pore space and flow towards the fracture. The gas was observed to flow comparably towards the fracture although production was somewhat higher near the well since this was where the pressure gradients were sharpest. A key observation made by Berawala et al. (2018) is that the adsorbed mass fraction increased towards the fracture region ($x \approx 0$) at a given time and also increased with time. This behavior was explained mathematically by using the Langmuir isotherm (see (41)):

$$\frac{\hat{a}_g(P_g)}{\hat{a}_g(P_g) + P_g} = \frac{\hat{a}_{max}}{\hat{a}_{max} + P_L + P_g} \tag{76}$$

From (76) it can be clearly seen that the fraction of adsorbed mass will increase when the pressure is reduced which explains the observed increase towards the fracture and with time (Berawala et al. 2018).

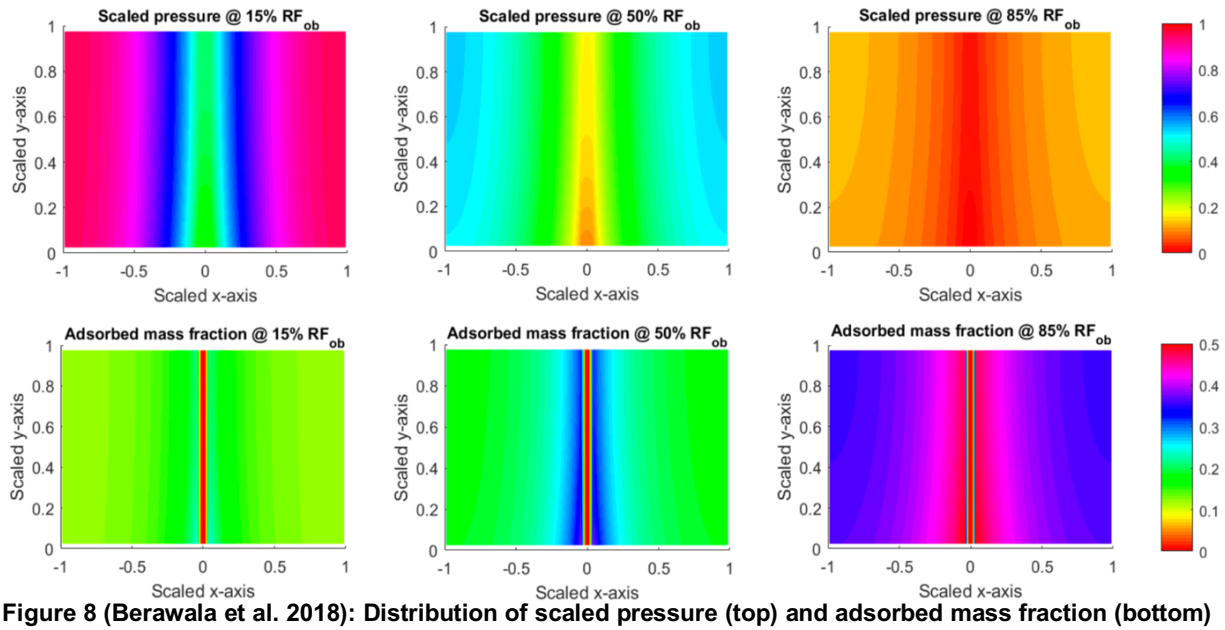

Figure 8 (Berawala et al. 2018): Distribution of scaled pressure (top) and adsorbed mass fraction (bottom) for the reference case at 15% (left), 50% (middle) and 85% (right) obtainable recovery RF_{ob}.The input parameters used were the same as those shown in Table 3 (excluding the high-effective-stress porosity).

4.3 Sensitivity Analysis

4.3.1 Demonstration of Geomechanical Effects

To demonstrate the effect of geomechanics on the model behaviour we use the four cases defined in **Table 4**. In these four cases the geomechanical parameters, or stress-dependence factors, η_m, Ψ_m and Ψ_f are varied. In the 'no geomechanics' case there are no geomechanical

effects considered and thus all three parameters η_m, Ψ_m and Ψ_f are equal to zero. The Marcellus shale 1, Marcellus shale 2 and Barnett shale cases, have geomechanical parameters η_m, Ψ_m and Ψ_f equal to the values used in simulation by Wang et al. (2017) when studying these three shales. All the other input parameters are kept constant and equal to the value given in **Table 3**.

Table 4: Four cases defined by the values given to the geomechanical parameters η_m, Ψ_m and Ψ_f ([1] Wang et al. 2017).

Case	$\eta_m\ (Pa^{-1})$	$\Psi_m(Pa^{-1})$	$\Psi_f(Pa^{-1})$
No geomechanics	0	0	0
[1] Marcellus shale 1	1.0e-09	5.0e-09	1.5e-08
[1] Marcellus shale 2	1.0e-09	5-0e-09	6.0e-08
[1] Barnett shale	2.0e-09	1.5e-08	8.5e-08

Figure 9 shows the gas recovery *RF* for up to 500 days for the cases listed in **Table 4**. We observe that the Marcellus shale 1, Marcellus shale 2 and Barnett shale cases all have lower gas recovery than the 'no geomechanics' case. For the Marcellus shale 1 and Marcellus shale 2 cases the gas recovery after 500 days is 1.74% and 5.33% lower, respectively. The difference is largest for the Barnett shale case, where gas recovery is 11.12% lower than the case with no geomechanics after 500 days of production.

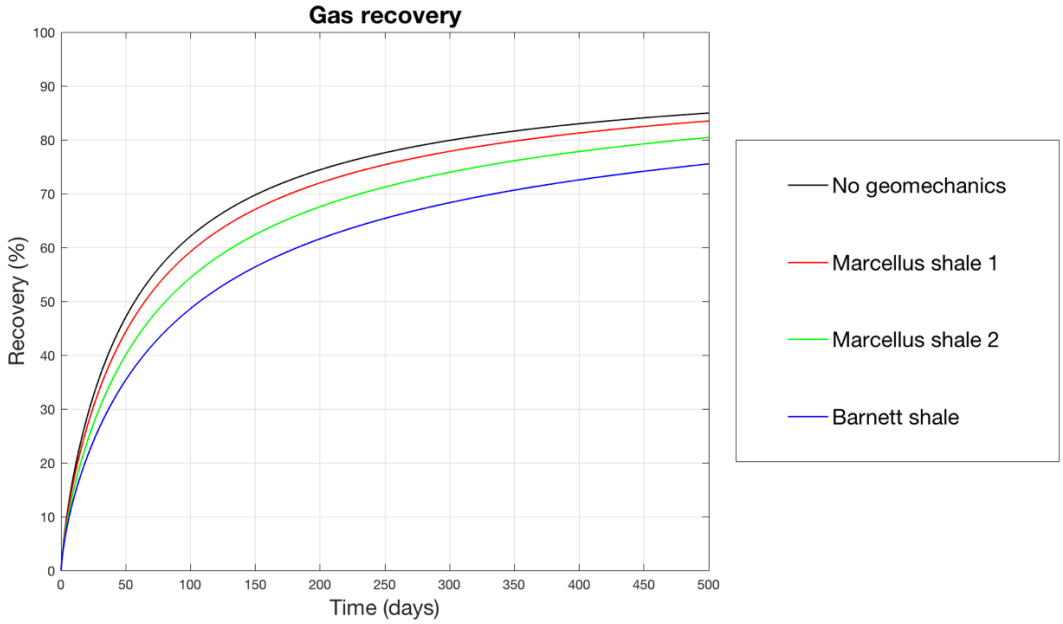

Figure 9: Effect of geomechanics on gas recovery RF for the four cases defined in Table 5. The geomechanical effects have largest impact in the Barnett shale case, resulting in a 11.12% decrease in gas recovery after 500 days of production.

When making observations in the next three figures (**Figure 10**, **Figure 11** and **Figure 12**) it is important to explain why the initial values of scaled average porosity and -permeability in the four cases are different. This does not mean that the initial absolute porosity and permeability of the formation have been changed from case to case. The difference in initial values comes from the definitions of the reference values ϕ_{ref} and K_{ref} (see (58)) which makes them dependent on the geomechanical parameters η_m, Ψ_m and Ψ_f as well as pressure P_g. As a result,

the scaled porosity and permeability will start at different values depending on how much they are changed during production. **Figure 10** shows how the scaled average matrix porosity is affected in the 'no geomechanics' case, the Marcellus shale 1 case, the Marcellus shale 2 case, and the Barnett shale case. The reduction in scaled average matrix porosity is seen to correlate with the size the matrix porosity-stress-dependence factor η_m. However, even though the Marcellus shale 1 and Marcellus shale 2 cases have the same value of η_m, there is a slightly larger reduction in the Marcellus shale 1 case.

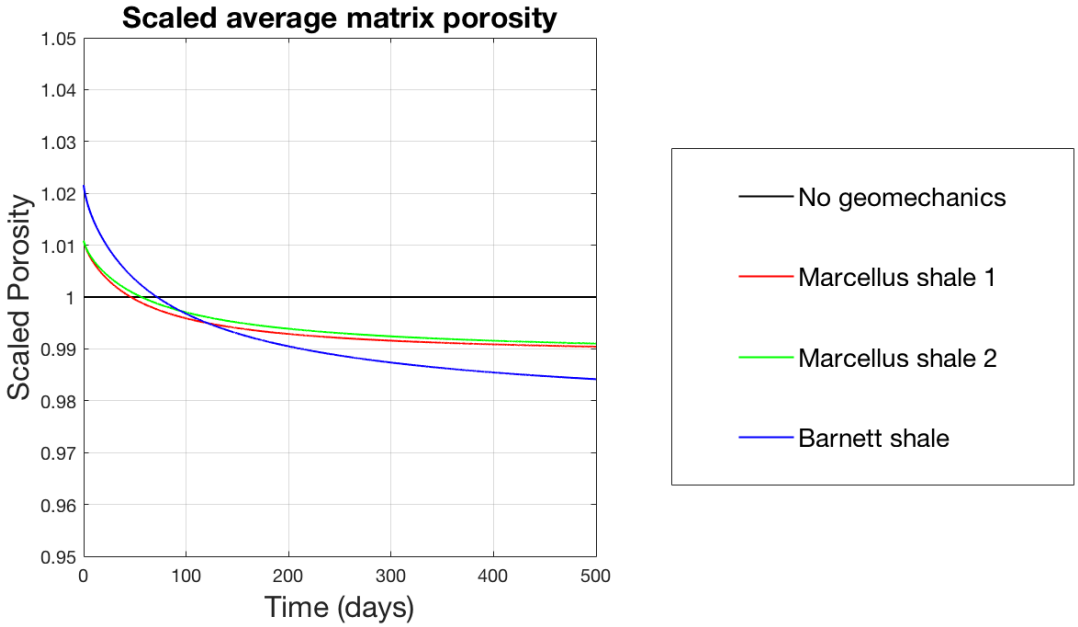

Figure 10: Effect of geomechanics on scaled average matrix porosity in the 'no geomechanics' case, the Marcellus shale 1 case, the Marcellus shale 2 case, and the Barnett shale case defined in Table 4.

Figure 11 shows how the scaled average matrix permeability is affected in the four cases. The same trends are observed as for the porosity. The Marcellus shale 1 case shows a slightly larger reduction in scaled average matrix permeability than the Marcellus shale 2 case when they are given the same value of Ψ_m. The scaled average fracture permeability is shown in **Figure 12**. To better illustrate the differences between the four cases, the y-axis has been chosen so that the initial values for the Marcellus shale 2 and Barnett shale case lie beyond the y-axis. The Barnett shale case has the highest reduction in scaled average fracture permeability, from 8.5870 to 0.6731.

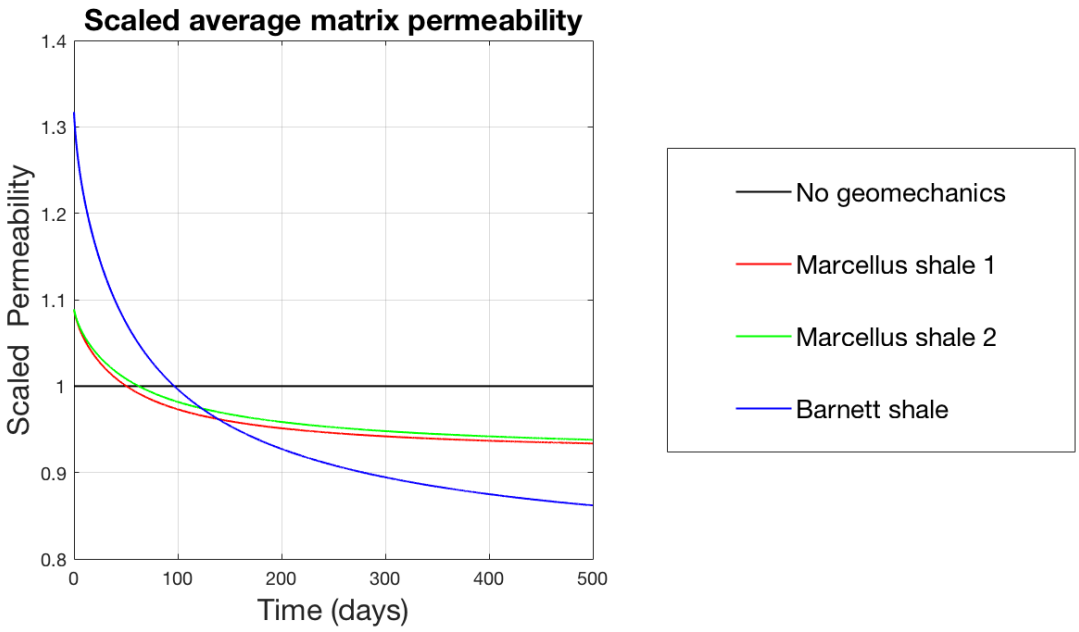

e 11: Effect of geomechanics on scaled average matrix permeability in the 'no geomechanics' case, arcellus shale 1 case, the Marcellus shale 2 case, and the Barnett shale case defined in Table 4.

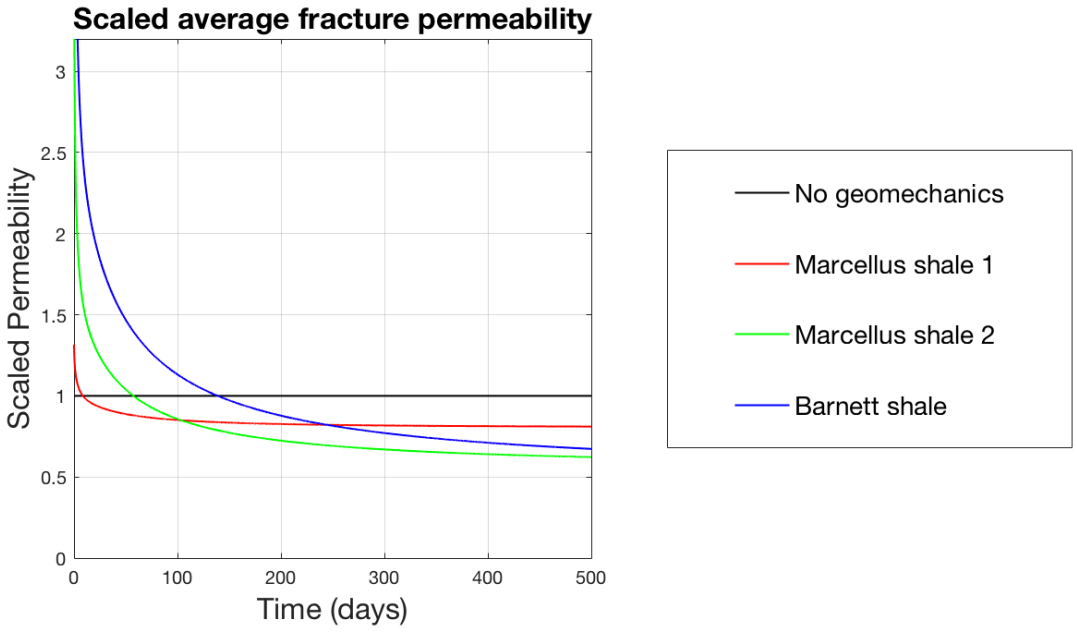

e 12: Effect of geomechanics on scaled average fracture permeability in the 'no geomechanics' case, arcellus shale 1 case, the Marcellus shale 2 case, and the Barnett shale case defined in Table 4. The values for Marcellus shale 2 and Barnett shale lie beyond the y-axis and are 4.0666 and 8.5870, ctively.

re 13 compares the scaled pressure distribution for the 'no geomechanics' case, the ellus shale 2 case, and the Barnett shale case at 15%, 50% and 85% of obtainable recovery RF_{ob}. To reach 15% obtainable recovery it takes the 'no geomechanics' case 6 days, the Marcellus shale 2 case 7 days, and the Barnett shale case 8 days. The difference in number of days needed to reach the same obtainable recovery increases with the obtainable recovery and is largest at 85%. To reach 85% obtainable recovery it takes the 'no geomechanics' case 194 days, the Marcellus shale 2 case 301 days, and the Barnett shale case 447 days. The pressure declines quickly in the fracture and is followed by gradual pressure decline in the surrounding matrix for all three cases. However, for the cases where geomechanical effects are considered,

ellus shale 2 (ıd Barnett shale case, the pressure declines faster in the areas closer ell (closer to $y = 0$) than in the areas further away from the well. This trend is most t 85% obtainable recovery.

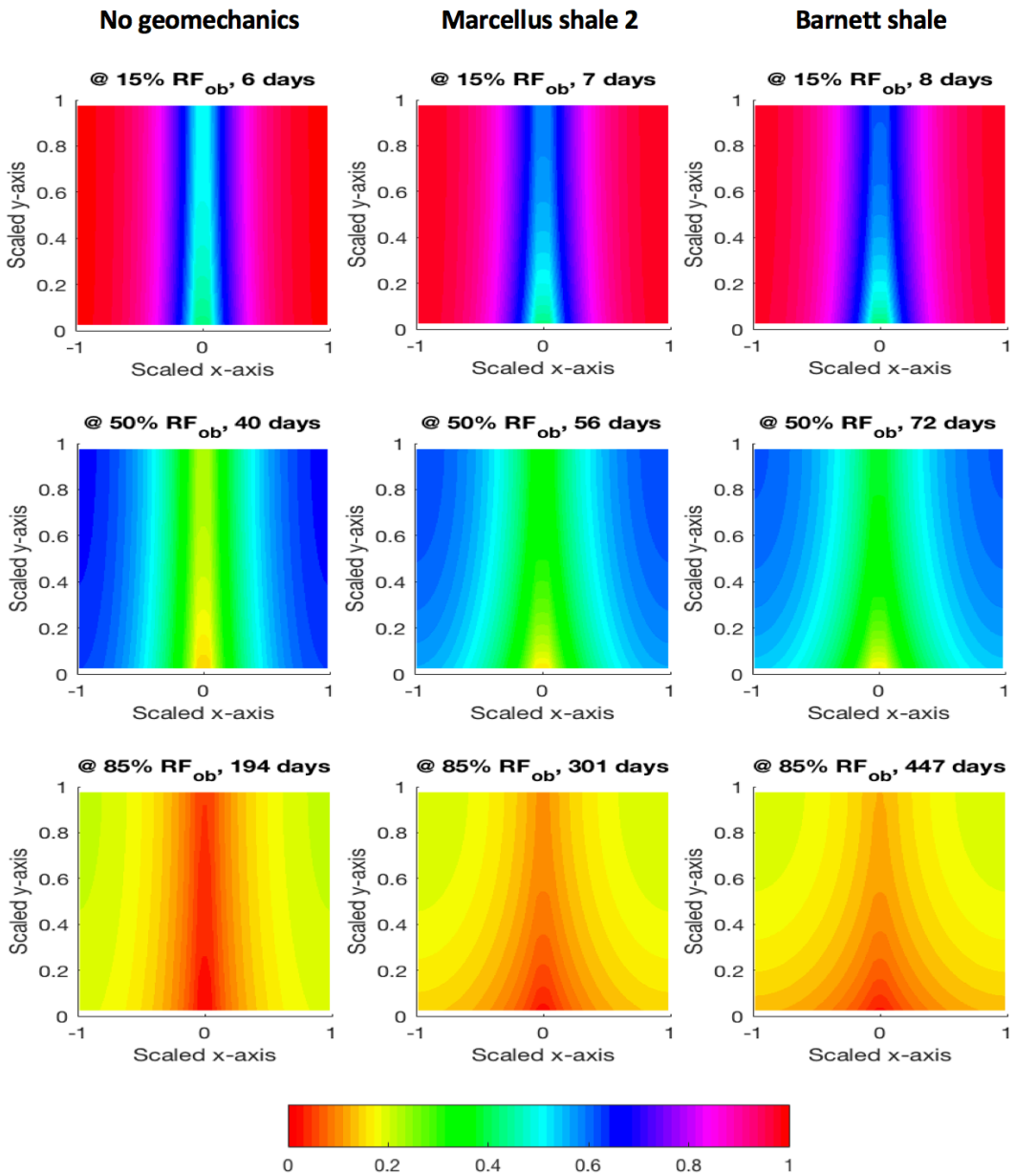

: Distribution of scaled pressure for the 'no geomechanics' case (left), Marcellus shale 2 case and Barnett shale case (right) at 15% (top), 50% (middle) and 85% (bottom) of obtainable recovery

14 compares the scaled porosity distribution for the 'no geomechanics' case, the ıs shale 2 case, and the Barnett shale case at 15%, 50% and 85% of obtainable recovery *RI* the 'no geomechanics' case the scaled porosity is equal to 1 in both fracture and matrix an ; not change during production. In the Marcellus shale 2 and Barnett shale case the sc: acture porosity is equal to 1 at all obtainable recoveries because the fracture porosity is ınsidered to be stress-dependent. The scaled porosity in the matrix for the Marcellus sh: ase and Barnett shale case is seen to decline faster in the areas closer to the well (closer to $y = 0$) than the areas further away from the well, most visibly at 50% obtainable recovery. Note that even though the initial scaled porosity in the Marcellus shale 2 case and Barnett shale case is higher than in the 'no geomechanics' case this does not mean that the initial absolute

of the matrix is higher. The higher values come from the definition of the reference ϕ_{ref} (see (58)) which makes the initial scaled porosity dependent on the matrix stress-dependence factor η_m and pressure P_g.

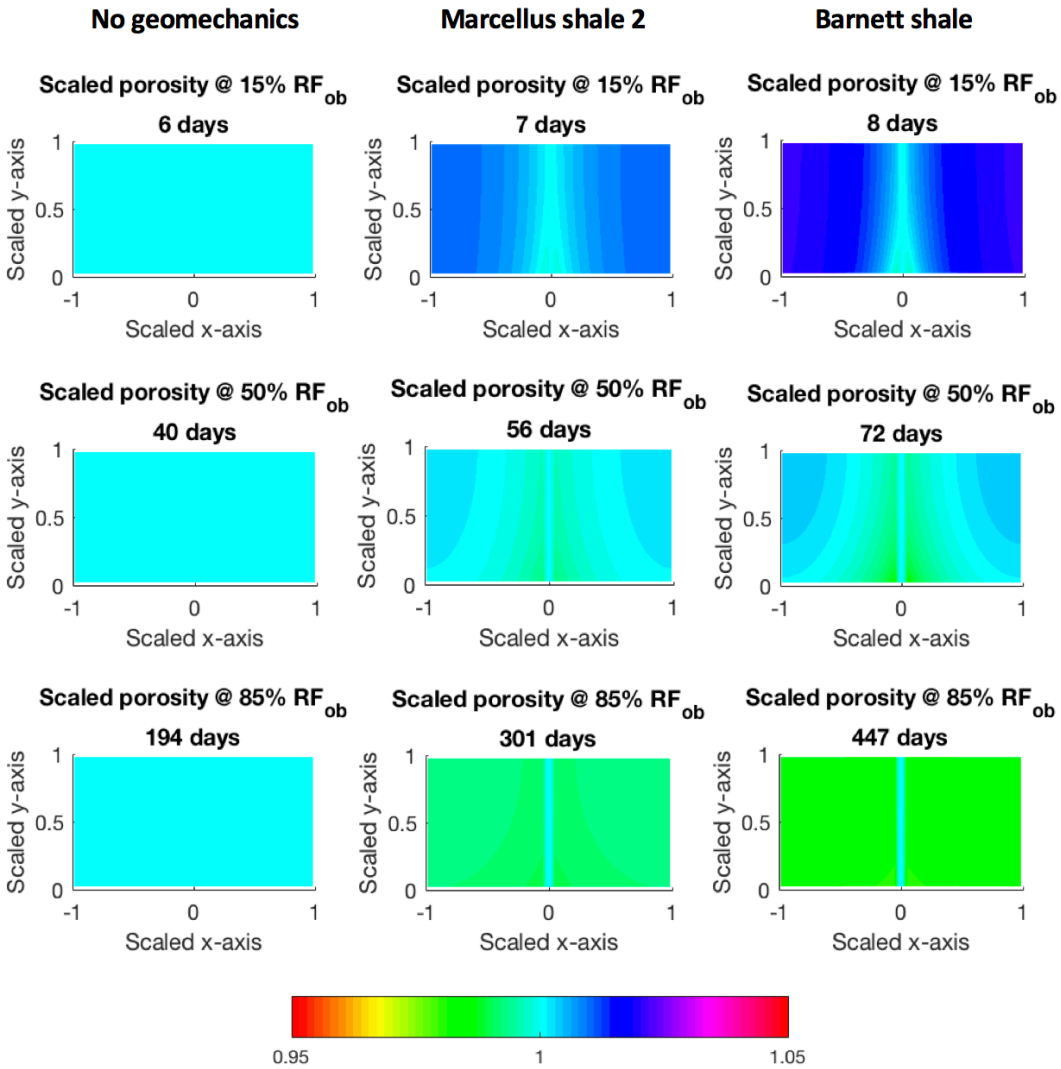

: Distribution of scaled porosity for the 'no geomechanics' case (left), Marcellus shale 2 case and Barnett shale case (right) at 15% (top), 50% (middle) and 85% (bottom) of obtainable recovery ne Marcellus shale 2 and Barnett shale cases, the matrix porosity is seen to decline faster in the ser to the well (closer to $y = 0$) than in the areas further away from the well.

5 compares the scaled permeability distribution for the 'no geomechanics' case, the s shale 2 case, and the Barnett shale case at 15%, 50% and 85% of obtainable recovery *RF* the 'no geomechanics' case the scaled permeability is equal to 1 in all areas of the res and does not change during production. In the Marcellus shale 2 case the decrease in ma ermeability is too small to be captured by the colourbar-scale and similarly in the Ba hale case there is only an observable decrease in scaled permeability at 15% obtainable rec , from around 1.4 to around 1.0. The scaled permeability in the fracture for the Ma s shale 2 case and Barnett shale case is seen to decline faster closer to the well (closer to $y = 0$) than further away from the well. Again, note that even though the initial scaled permeabilities in the Marcellus shale 2 case and Barnett shale case are higher than in the 'no geomechanics' case this does not mean that the initial absolute permeability is higher. The higher values come from the definition of the reference permeability K_{ref} (see (58)) which

makes the initial scaled permeability dependent on the permeability-stress-dependence factors Ψ_m, Ψ_f and pressure P_g.

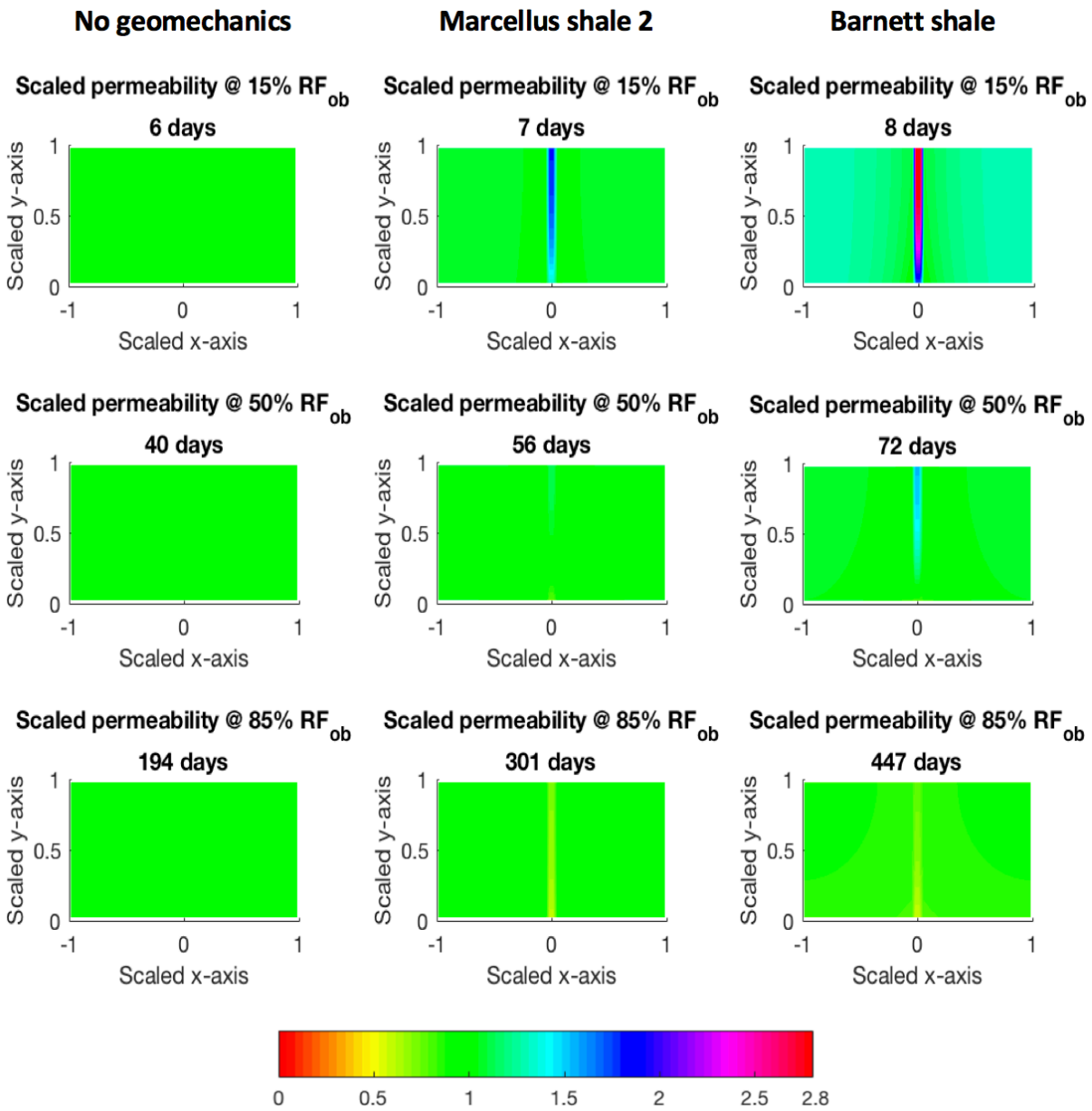

Figure 15: Distribution of scaled permeability for the 'no geomechanics' case (left), Marcellus shale 2 case (middle), and Barnett shale case (right) at 15% (top), 50% (middle) and 85% (bottom) of obtainable recovery RF_{ob}.

4.3.2 Role of Fracture Size and Geomechanical Effects

In this section we will investigate the effect that fracture size and individual geomechanical effects have on the gas recovery RF. To achieve this, five new cases are defined in Table 5 in which some geomechanical parameters are ignored while other are considered. In case 1 only the stress-dependent fracture permeability (Ψ_f) is included. Case 2 is a case where only stress-dependent matrix permeability (Ψ_m) is included. In case 3 both Ψ_f and Ψ_m are included while stress-dependent matrix porosity is ignored. Lastly, case 4 is a case where all three geomechanical effects are considered (η_m, Ψ_f and Ψ_m). For each of the five cases there are

two different fracture sizes compared where the average fracture width (b_0) is changed from 0.05 m to 0.009 m. All other input parameters are kept constant and equal to the values given in Table 3.

Table 5: Five cases defined by the values given to the geomechanical parameters η_m, Ψ_m and Ψ_f.

Case	$\eta_m\ (Pa^{-1})$	$\Psi_m(Pa^{-1})$	$\Psi_f(Pa^{-1})$
No geomechanics	0	0	0
Case 1	0	0	8.5e-08
Case 2	0	1.5e-08	0
Case 3	0	1.5e-08	8.5e-08
Case 4	2.0e-09	1.5e-08	8.5e-08

Figure 16 shows the gas recovery RF for up to 500 days for all the cases with varied fracture size and geomechanical effects. When comparing cases with the same values of geomechanical parameters (same colours), gas recovery is consistently higher for cases where the average fracture width is high, given by $b_0 = 0.05$ m. At this larger fracture size, the gas recovery profiles for Case 1 and Case 2 are similar, both resulting in approximately 4.01% lower recovery than the 'no geomechanics' case after 500 days. However, for the smaller fracture size ($b_0 = 0.009$ m) the gas recovery profiles for Case 1 and Case 2 are no longer similar. Case 1 now results in a decrease in recovery of around 13.81% while Case 2 results in a decrease of around 3.66% compared to the 'no geomechanics' case.

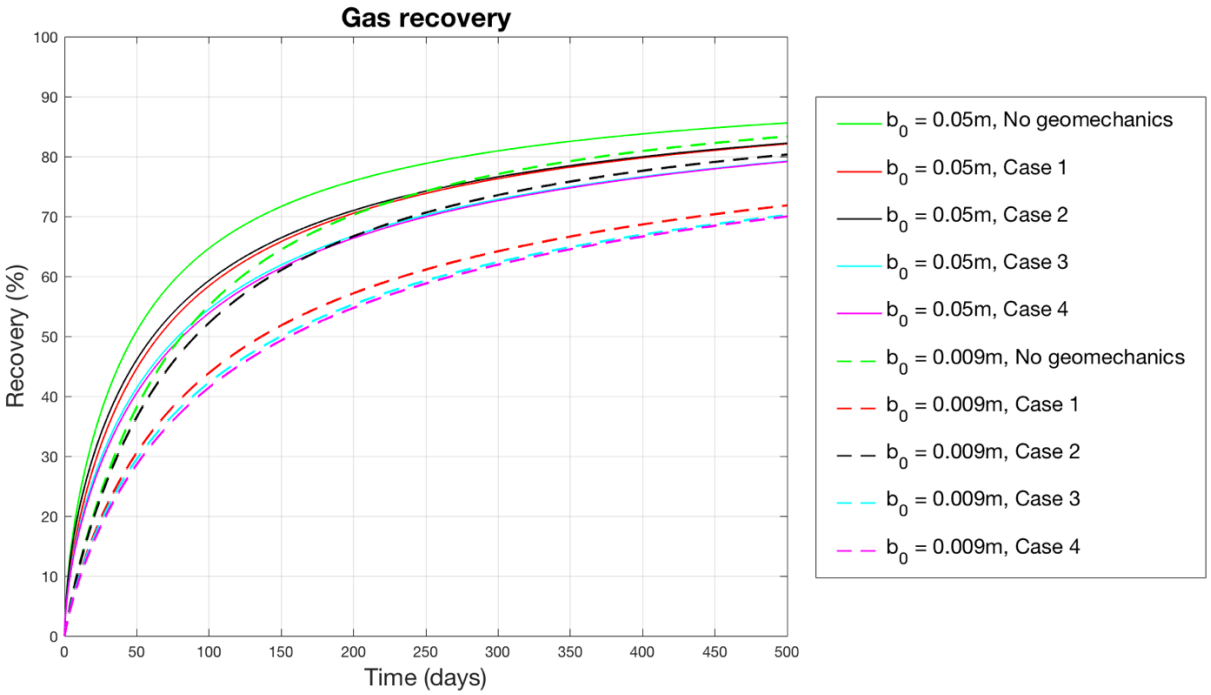

Figure 16: Effect of fracture size (b_0) and geomechanical effects (η_m, Ψ_f and Ψ_m) on gas recovery RF.

4.3.3 Role of Fracture Shape and Geomechanical Effects

In this section we will investigate the effect that fracture shape and individual geomechanical effects have on the gas recovery RF. For representing varying geomechanical effects the five cases defined in Table 5 are used. For each of the five cases there are two different fracture shapes considered by changing the $\frac{b_{max}}{b_{min}}$ ratio is from 1 to 10. A $\frac{b_{max}}{b_{min}}$ ratio of 1 indicates that the fracture has uniform width along the y-axis whereas a ratio of 10 indicates that the fracture is 10 times narrower at $y = L_y$ compared to at $y = 0$. The average fracture width b_0 = 0.02 m for all cases. All other input parameters are kept constant and equal to the values given in Table 3. To investigate how fracture shape and geomechanical effects impact on gas recovery at a smaller fracture size there will be similar comparisons made where the average fracture width b_0 = 0.009 m for all cases. All other input parameters are kept constant and equal to the values given in **Table 3**. **Figure 17** shows the gas recovery RF for up to 500 days for the cases with varied fracture shape and geomechanical effects when the average fracture width b_0 is 0.02 m. We observe that the cases with the same geomechanical parameters (same colours) are very similar for both $\frac{b_{max}}{b_{min}} = 1$ and $\frac{b_{max}}{b_{min}} = 10$. For the 'no geomechanics' case and Case 2 it takes slightly longer time to reach the same recovery when fracture shape is given by $\frac{b_{max}}{b_{min}} = 10$. For Case 1, Case 3 and Case 4 this is reversed, it takes slightly longer time to reach the same recovery when fracture shape is given by $\frac{b_{max}}{b_{min}} = 1$.

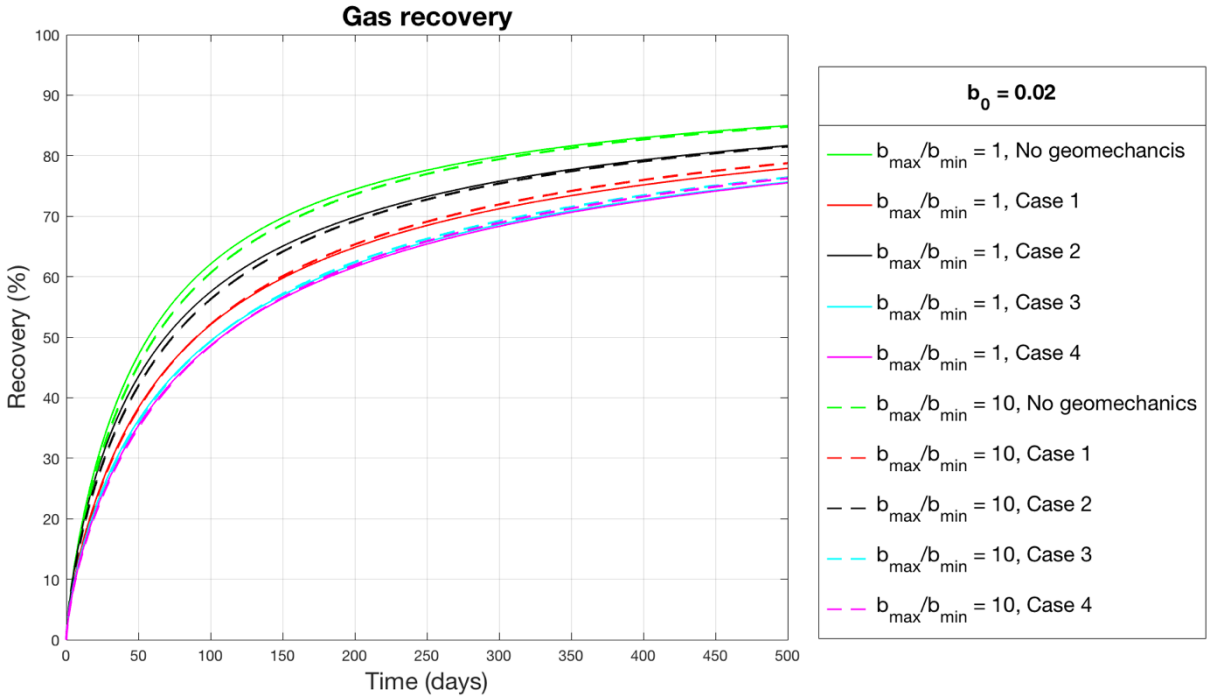

Figure 17: Effect of fracture shape and geomechanical effects on gas recovery RF when the average fracture width b_0 is 0.02 m. The fracture shape is varied by changing the $\frac{b_{max}}{b_{min}}$ ratio from 1 to 10 and geomechanical effects are varied as defined in Table 5.

Figure 18 shows the gas recovery RF for up to 500 days for the cases with varied fracture shape and geomechanical effects when the average fracture width b_0 is 0.009 m. Similar trends are observed as in **Figure 17**. However, it is seen that the recovery for the 'no geomechanics' case

and Case 2 is slightly more affected by fracture shape when the average fracture width is lower ($b_0 = 0.009$ m).

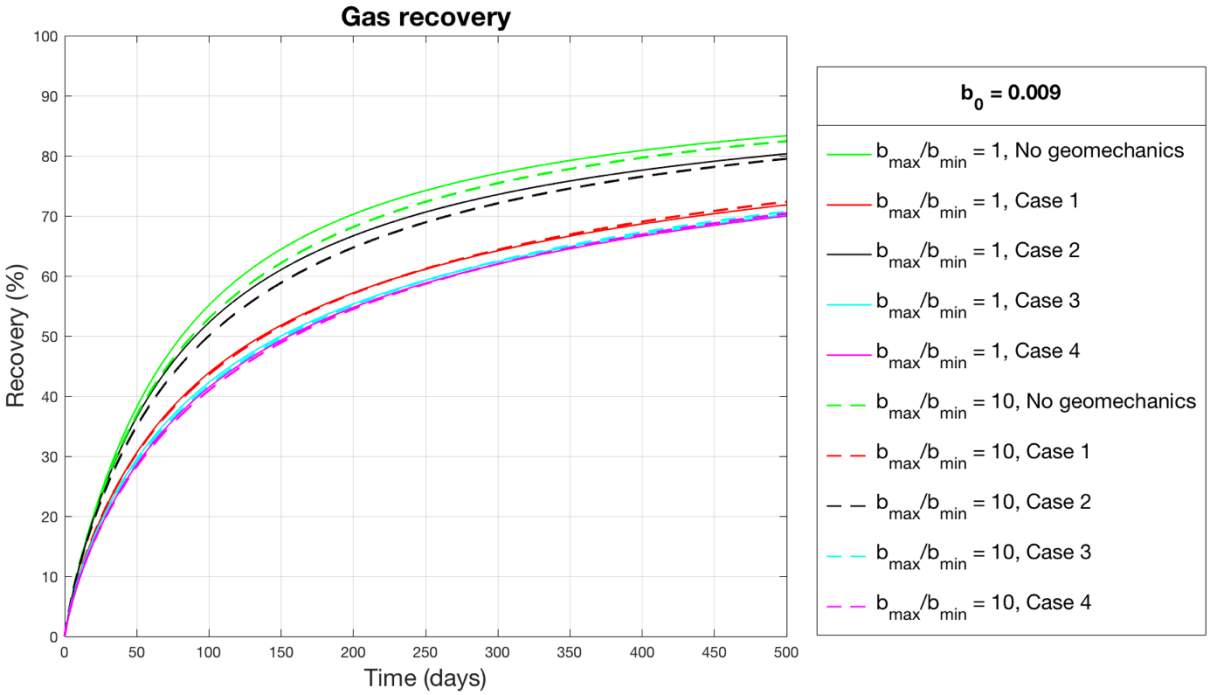

Figure 18: Effect of fracture shape and geomechanical effects on gas recovery RF when the average fracture width b_0 is 0.009 m. The fracture shape is varied by changing the $\frac{b_{max}}{b_{min}}$ ratio from 1 to 10 and geomechanical effects are varied as defined in Table 5.

4.3.4 Role of Fracture Spacing and Geomechanical Effects

In this section we will investigate the effect that fracture spacing and individual geomechanical effects have on the gas recovery RF. For representing varying geomechanical effects the five cases defined in Table 5 are used. For each of the five cases there are three different fracture spacings considered by changing the matrix half-length (L_x) from 7 m to 15 m and 35 m. All other input parameters are kept constant and equal to the values given in **Table 3**. **Figure 19** shows the gas recovery RF for up to 500 days for the cases with varied fracture spacing and geomechanical effects. When comparing the cases where only matrix permeability is considered stress-dependent (Case 2's, black curves) to the 'no geomechanics' cases (green curves) the difference between them are seen to increase as fracture spacing increases. At $L_x = 7$ m, case 2 results in a decrease of around 0.01% in gas recovery compared to the 'no geomechanics' case. At $L_x = 15$ m, case 2 results in a decrease of around 1.48% in gas recovery compared to the 'no geomechanics' case. And at $L_x = 35$ m, case 2 results in a decrease of around 5.71% in gas recovery compared to the 'no geomechanics' case.

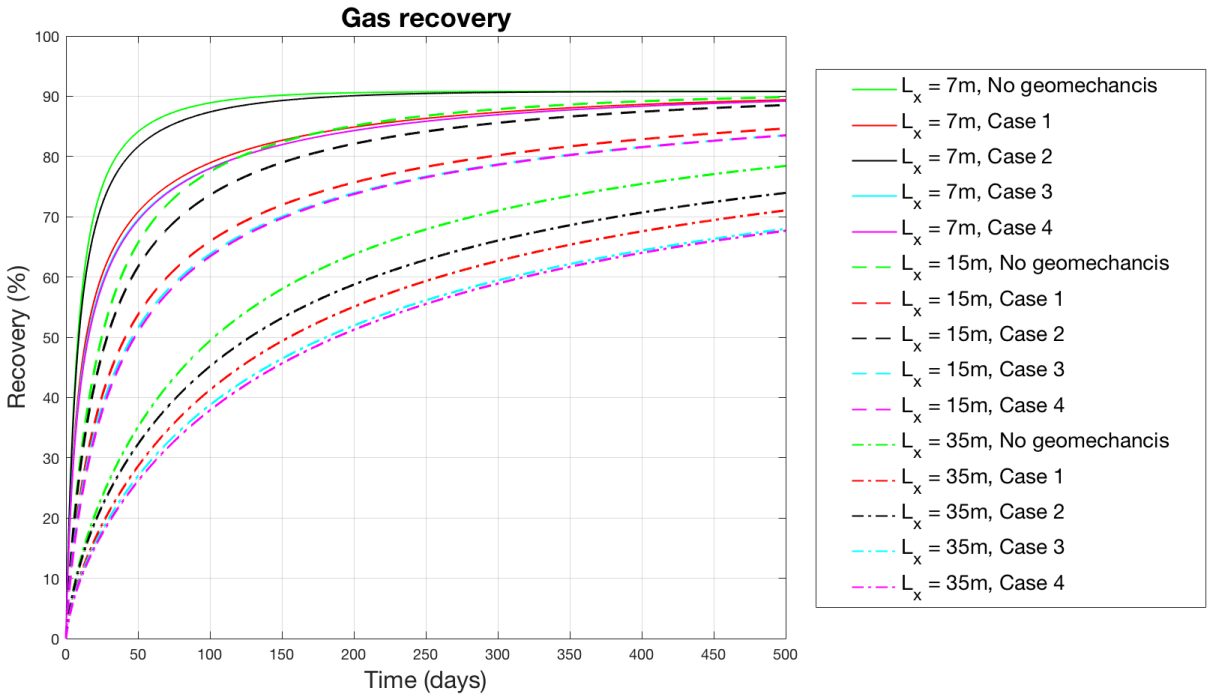

Figure 19: Effect of fracture spacing and geomechanical effects on gas recovery RF. The fracture spacing is varied by changing the average matrix half-length L_x from 7 m to 15 m and 35 m and geomechanical effects are varied as defined in Table 5.

4.3.5 Role of Initial Reservoir Pressure and Geomechanical Effects

In this section we will investigate the effect that initial reservoir pressure and individual geomechanical effects have on the gas recovery RF. For representing varying geomechanical effects the five cases defined in **Table 5** are used. For each of the five cases there are two different initial reservoir pressures considered by changing P_{init} from 300 bar to 700 bar. All other input parameters are kept constant and equal to the values given in **Table 3**. **Figure 20** shows the gas recovery RF for up to 500 days for the cases with varied initial reservoir pressure and geomechanical effects. It shows that the effects from geomechanics on gas recovery are larger, in general, for an initial reservoir pressure $P_{init} = 700$ bar than for $P_{init} = 300$ bar. Other comparisons made from this figure may not be accurately made because when P_{init} is changed this will also change the amount of adsorbed and free gas originally in place in the matrix, see **Appendix A)**.

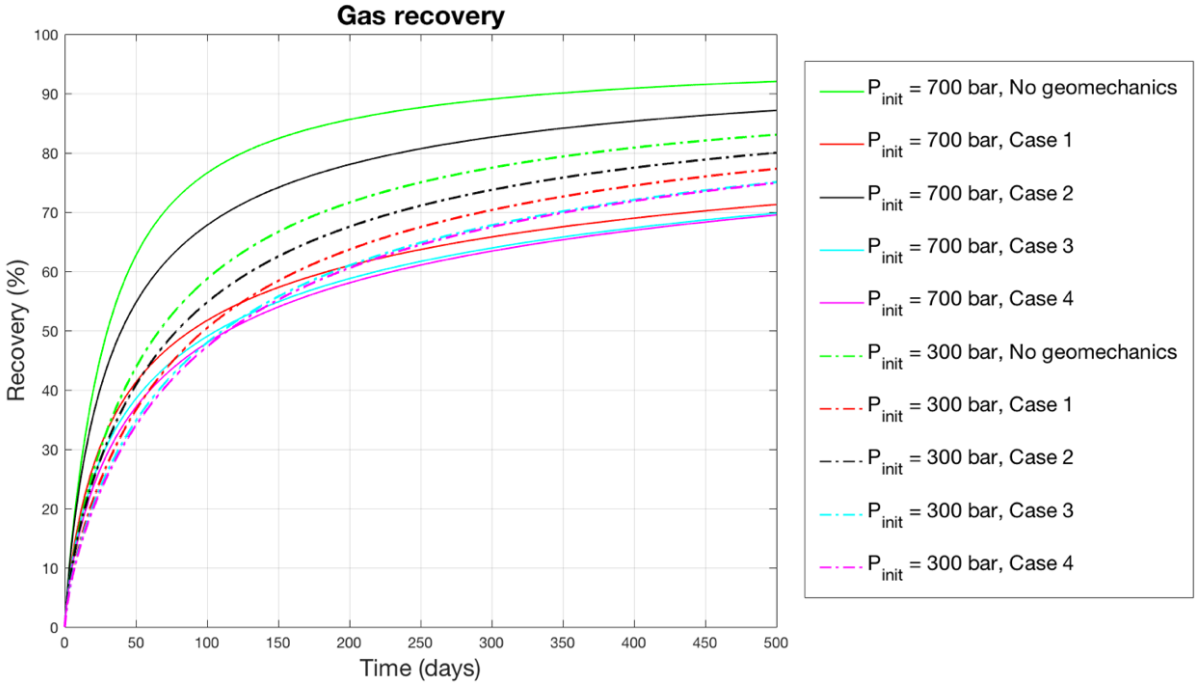

Figure 20: Effect of initial reservoir pressure and geomechanical effects on gas recovery RF. The initial reservoir pressure is varied from $P_{init} = 300\ bar$ to $P_{init} = 700\ bar$ and geomechanical effects are varied as defined in Table 5.

5. Discussion

5.1 Interpretation of Results

In the previous chapter and particularly in section 4.3.1 we saw results demonstrating the effect that geomechanics have on scaled recovery and properties like pressure, porosity and permeability. Increasing the stress-dependence factors η_m, Ψ_m and Ψ_f resulted in larger reductions in gas recovery. The scaled average matrix porosity and scaled average matrix permeability in the Marcellus shale 1 case was affected slightly more than in the Marcellus shale 2 case even though they had the same values of η_m and Ψ_m. This indicates that the fracture permeability-stress-dependence factor Ψ_f will influence the impact of these two properties. This can be explained by the scaled permeability distribution plots in **Figure 15** where we observed that the fracture permeability decreases faster in the areas closer to the well perforation which will affect matrix properties. In **Figure 13** we make similar observations for the scaled pressure distribution plots. This shows that the fracture permeability reduction and pressure reduction in the reservoir are affecting each other through coupled processes. The scaled matrix porosity and matrix permeability are also part of this coupling, indicated by **Figure 14**. These three figures indicate that stress-dependent matrix porosity, stress-dependent matrix permeability and stress-dependent fracture permeability all cause a delayed pressure reduction in the areas further away from the well perforation. Therefore, the geomechanical effects reduce the driving force of gas production from the matrix to the fracture, and from the fracture to the well by creating local pressure buildups in regions furthest away from the well perforation.

When investigating the effect of changing fracture size with geomechanical effects a key observation was made in **Figure 16**. The fracture permeability reduction had the most impact on gas recovery out of all the geomechanical effects. This indicates that the stress-dependence of fracture permeability becomes more important at smaller average fracture width and the gas recovery will be more sensitive to Ψ_f. When the effect of fracture shape and geomechanical effects was investigated, very similar gas recoveries were seen in **Figure 17**, indicating that the fracture shape has low impact on gas recovery. However, when making the same investigation at a lower fracture size ($b_0 = 0.009$ m) in **Figure 18**, the gas recovery for Case 2 became more sensitive to fracture shape. This tells us that at lower fracture sizes, and when the stress-dependence of matrix permeability is high, the fracture shape has more significant impact on gas recovery. In **Figure 19** the impact on gas recovery from varying fracture spacing and geomechanical effects is shown. We found that for longer fracture spacing ($L_x = 35$ m) the gas recovery is more sensitive to the stress-dependent matrix permeability, resulting in a 5.71% decrease in recovery, compared to a 0.01% decrease at $L_x = 7$ m. This observation is in agreement with findings made by Wang et al. (2017) which were illustrated in **Figure 5**. Similarly, they found that Marcellus shale no. 1 was most sensitive to changes in matrix permeability-stress-dependence factor and based it on the fact that it was the case with lowest fracture density (largest fracture spacing). Finally, in **Figure 20** we observed that the impact from geomechanics is largest at higher initial reservoir pressure P_{init}. This comes from the fact that the porosity and permeability can be considered functions of effective stress. A larger initial reservoir pressure results in higher effective stress in the formation as the pressure declines towards the bottom hole well pressure P_{well}.

5.2 Interpretation of Results using Dimensionless Numbers

The effect that geomechanics and other reservoir properties have on gas recovery has been demonstrated. In the following the model behaviour is interpreted by using the scaled model (64) and (65). If we assume that in a uniform fracture there is an initial scaled pressure is $P' = 1$ which diffuses towards zero, the time required for this process will be approximately τ^f. Similarly, the time required for diffusing free and adsorbed gas out of the matrix from $P' = 1$ to $P' = 0$ will be reflected by the time scale τ^m, given that the open boundary to the fracture has scaled pressure equal to zero. To be produced, all the gas from the matrix has to flow through the fracture. This process will at minimum require a time of $(\beta + 1)\tau^f$ where the factor $(\beta + 1)$ signifies that there is β times as much gas in the matrix as in the fracture in addition to the fracture volume. If the time $(\beta + 1)\tau^f$ is significant compared to the time τ^m the diffusion of gas from the matrix may be delayed. Noting that $\beta \gg 1$ we introduce the ratio ω of these times as:

$$\omega = \frac{(\beta + 1)\tau^f}{\tau^m} \approx \alpha\beta = \frac{L_y^2 K_{ref}^m}{L_x b_0 K_{ref}^f} \tag{77}$$

If $\omega \ll 1$ it means that the gas has negligible residence time in the fracture and gas flow is completely controlled by the time scale of diffusion from the matrix. We can therefore expect a unique behaviour for cases where $\omega \ll 1$ when plotting recovery vs. time scaled against τ^m. As ω becomes larger the residence time of gas in the fracture becomes more significant and delays the gas diffusion process. According to (77) the only parameters affecting this process under the stated assumptions are the reference permeabilities (K_{ref}^m and K_{ref}^f), the fracture spacing ($2L_x$), the fracture half-width (b_0) and the fracture length (L_y).

5.2.1 Systematic Variations of Alpha and Beta

In this section, 20 simulation cases of gas recovery will be presented and interpreted according to the dimensionless number $\omega = \alpha\beta$. Input parameters have been varied in simulation cases so that the product $\alpha\beta$ is equal to 10^{-3}, 10^{-2}, 10^{-1} and 10^{0}. For each of the $\alpha\beta$ values constant parameters appearing in α and β have been varied, such as fracture spacing ($2L_x$), fracture half-width (b_0) and fracture length (L_y). Parameters that vary spatially and during the recovery process, such as matrix and fracture permeabilities, are represented by reference values in α and β (K_{ref}^m *and* K_{ref}^f). For every case, unless stated otherwise, geomechanics are considered by using the stress-dependence factors for the Barnett shale case listed in **Table 4**. Three special scenarios are considered: 1) No geomechanics considered (all three stress-dependence factors, η_m, Ψ_m and Ψ_f are equal to zero); 2) High fracture-width ratio ($\frac{b_{max}}{b_{min}} = 10$); 3) High initial reservoir pressure $P_{init} = 700$ bar compared to the reference case $P_{init} = 344.7$ bar. The resulting 20 simulation cases are presented in terms of gas recovery vs. time in **Figure 21** (top left). It is seen that the recovery profiles are very different for all cases and they span a wide range in the time scale. In **Figure 21** (bottom) the same simulations are presented in terms of obtainable recovery RF_{ob} vs. time scaled against τ^m. We observe that when comparing the cases with geomechanics, where only constant parameters appearing in α and β have been varied (indicated by full lines), to the cases where there are no geomechanics considered (indicated by dashed lines) the curves group well at $\alpha\beta = 10^{-3}$ and $\alpha\beta = 10^{-2}$. Naturally, there is a slightly higher recovery obtained for the cases without geomechanics.

At $\alpha\beta = 10^{-1}$ and $\alpha\beta = 1$ the widest green curve and widest yellow curves vary significantly from the rest of the curves with the same value of $\alpha\beta$. This indicates that the fracture properties have become more important for recovery and the effect from geomechanics is significant.
At the low values of $\alpha\beta$ the residence time of gas in the fracture is insignificant compared to the matrix and the recovery will only depend on matrix properties. The effect from geomechanics are not as large for these low values. This is also why the cases where the fracture shape is varied using $\frac{b_{max}}{b_{min}} = 10$ (indicated by dotted lines) show similar curves in **Figure 21** (bottom). Cases where the initial reservoir pressure has been increased (indicated by dash-dotted lines) show similar curves for low values of $\alpha\beta$. Only at $\alpha\beta = 1$ is the difference significant, and the obtainable recovery is observed to be much higher up until around $\frac{t}{\tau^m} = 1.6$.

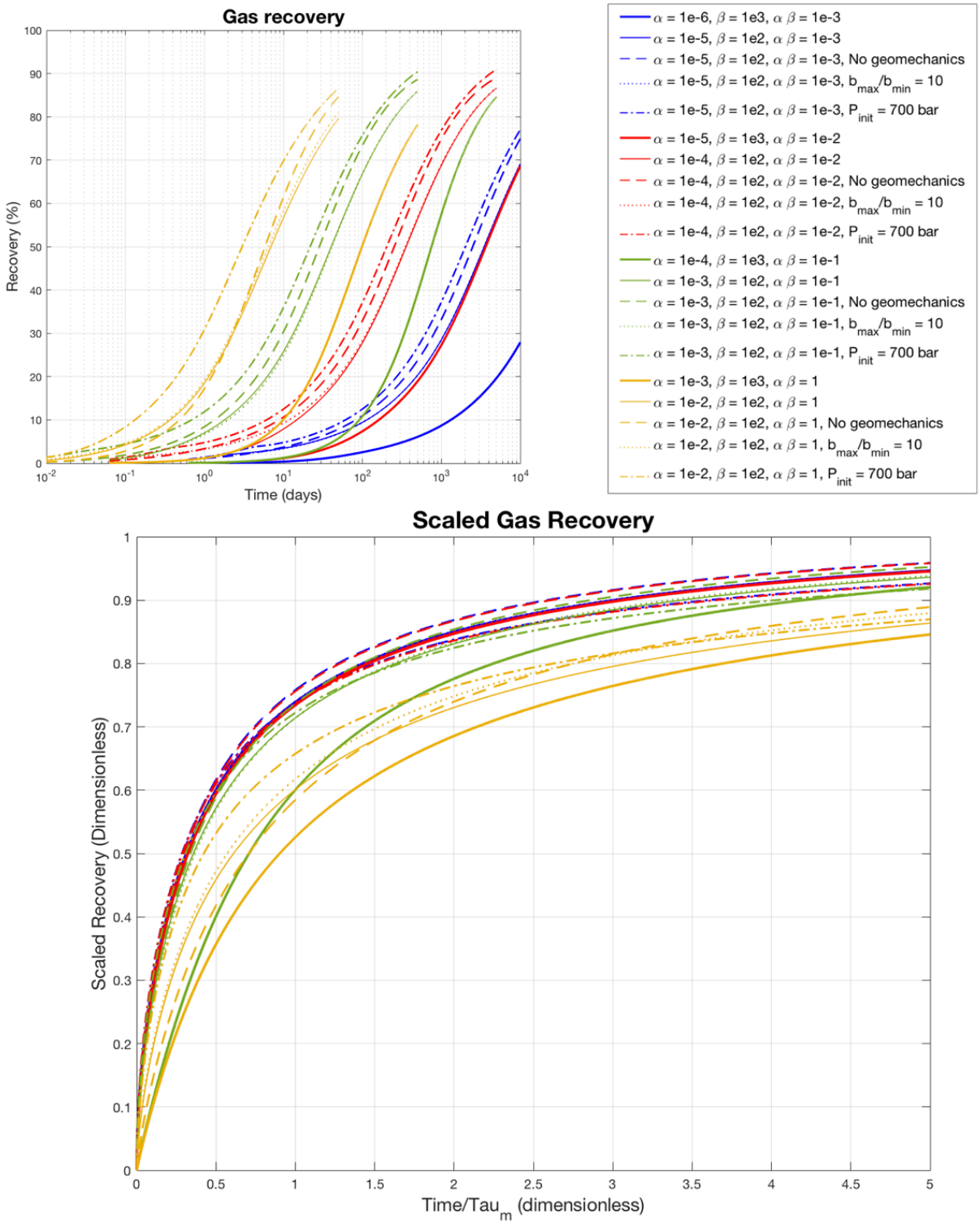

Figure 21: Absolute (top left) and scaled (bottom) gas recovery for 20 cases where $\omega = \alpha\beta$ is constant for the values: 10^{-3}, 10^{-2}, 10^{-1} and 10^{0}. Parameters α, β, b_{max}/b_{min}, K^{f}_{ref} and K^{m}_{ref} are varied in the 20 cases. Any unspecified parameter is given in Table 3.

References

Aguilera, R. (2002). Incorporating Capillary Pressure, Pore Throat Aperture Radii, Height Above Free Water Table, and Winland r35 Values on Pickett Plots. *AAPG Bulletin*, **86**, 605-624.

Alnoaimi, K. R. and Kovscek, A. R. (2013). *Experimental and Numerical Analysis of Gas Transport in Shale Including the Role of Sorption*. Paper presented at the SPE Annual Technical Conference and Exhibition.

Alramahi B, Sundberg M. I. (2012). *Proppant Embedment and Conductivity of Hydraulic Fractures in Shales*. ARMA conference paper presented at the 46th US rock mechanics/geomechanics symposium.

Ambrose, R. J., Hartman, R. C., Diaz-Campos, M., Akkutla, I. Y., and Sondergeld, C. H. (2012). Shale Gas-in-Place Calculations Part I: New Pore-Scale Considerations. *SPE Journal*, **17**(1).

Andersen, P., Evje, S., Kleppe, H. (2014). A model for spontaneous imbibition as a mechanism for oil recovery in fractured reservoirs. *Transport in Porous Media*, **101**(2), 299-331.

Andersen, P. Ø., Evje, S., Kleppe, H., Skjæveland, S. M. (2015). A Model for Wettability Alteration in Fractured Reservoirs. *SPE Journal*, **20**(6), 1-261.

Berawala, D. S., Andersen, P. Ø., and Ursin, J. R. (2018). *Controlling Parameters for Shale Gas Production Into a Well-Induced Fracture: A Fracture-Matrix Modelling Approach.* Paper presented at the SPE 80th EAGE Annual Conference & Exhibition.

Berawala, D. S., Ursin, J. R., & Slijepcevic, O. (2017). Sphere in Cube Grid Approach to Modelling of Shale Gas Production Using Non-Linear Flow Mechanisms. *World Academy of Science, Engineering and Technology, International Journal of Geological and Environmental Engineering*, **4**(9).

Beskok, A. and Karniadakis, G. E. (1999). A Model for Flows in Channels, Pipes, and Ducts at Micro and Nano Scales. *Microscale Thermophysical Engineering*, **3**(1), 43-77.

Blasingame, T. A. (2008). *The Characteristic Flow Behavior of Low-Permeability Reservoir Systems*. Paper presented at the SPE unconventional reservoirs conference.

Brunauer, S., Emmet, P. H. and Teller, E. (1938). Adsorption of Gases in Multimolecular Layers. *Journal of the American Chemical Society*, **60**(2). 309-319.

Bustin, R. M., Bustin, A. M. M., Cui, A., Ross, D., and Pathi, V. M. (2008). *Impact of Shale Properties on Pore Structure and Storage Characteristics.* Paper presented at the SPE Shale Gas Production Conference.

Cipolla, C. L., Lolon, E. P., Erdle, J. C., and Rubin, B. (2010). Reservoir Modeling in Shale-Gas Reservoirs. *SPE Reservoir Evaluation & Engineering*, **13**(4), 638-653.

Civan, F., Rai, C. S., and Sondergeld, C. H. (2011). Shale-Gas Permeability and Diffusivity Inferred by Improved Formulation of Relevant Retention and Transport Mechanisms. *Transport in Porous Media*, **86**(3), 925-944.

Cook, J. (2015). The Defining Series; Geomechanics. *Oilfield Review*.

Cui, X., Bustin, A. M. M. and Bustin, R. M. (2009). Measurements of Gas Permeability and Diffusivity of Tight Reservoir Rocks: Different Approaches and Their Applications. *Geofluids*, **9**(3), 208-223.

Curtis, J.B. (2002). Fractured Shale-Gas Systems. *AAPG Bulletin*, **86**(11), 1921-1938.

Darcy, H. (1856). *Les Fontaines Publiques de la Ville Dijon*. Dalmont.

Davies, J. P. and Davies, D. K. (1999). Stress-Dependent Permeability Characterization and Modeling. *SPE Journal*, **6**(2).

Dong, Z., Holditch, S. A. and McVay, D. A. (2012). *Resource Evaluation for Shale Gas Reservoirs*. Paper presented at the SPE Hydraulic Fracturing Technology Conference.

Evans R. D., Civan F. (1994). *Characterization of Non-Darcy Multiphase Flow in Petroleum Bearing Formations*. Report, US DOE Contract No. DE AC22-90BC14659.

Fan L, Thompson J. W., Robinson JR. (2010). *Understanding Gas Production Mechanism and Effectiveness of Well Stimulation in the Haynesville Shale Through Reservoir Simulation*. CSUG/SPE paper presented at the Canadian unconventional resources and international petroleum conference.

Fathi, E. and Akkutlu, I. Y. (2013). Lattice Boltzmann Method for Simulation of Shale gas Transport in Kerogen. *SPE Journal,* **18**(1). 27-37.

Franquet, J. A., Mitra, A., Warrington, D. S., Moos, D., and Lacazette, A. (2011). *Integrated Acoustic, Mineralogy, and Geomechanics Characterization of the Huron Shale, Southern West Virginia, USA.* Paper presented at the Canadian Unconventional Resources Conference.

Gao C, Lee J. W, Spivey J. P, Semmelbeck M. E. (1994). *Modeling Multilayer Gas Reservoirs Including Sorption Effects*. Paper presented at the SPE eastern regional conference and exhibition.

Guo, C. H., Wei, M. Z., Chen, H. W., He, X., and Bai, B. (2014). *Improved Numerical Simulation for Shale Gas Reservoirs*. Paper presented at the Offshore Technology Conference-Asia.

Haghshenas, B., Clarkson, C. R. and Chen, S. (2013). *Multi-Porosity Multi-Permeability Models for Shale Gas Reservoirs.* Paper presented at the SPE Unconventional Resources Conference in Canada.

Hellmann, J. R., Scheetz, B. E., Luscher, W. G., Hartwich, D. G. and Koseki, R. P. (2014). Proppants for Shale Gas and Oil Recovery; Engineering Ceramics for Stimulation of Unconventional Energy Resources. *American Ceramic Society Bulletin*, **93**(1), 28.

I. Langmuir. (1918). The Adsorption of Gases on Plane Surfaces of Glass, Mica and Platinum. *Journal of the American Chemical Society*, **40**, 1403-1461.

Kamenov, A., Zhu, D., Hill, A. D. and Zhang, J. (2013). *Laboratory Measurement of Hydraulic Fracture Conductivities in the Barnett shale*. Paper presented at the SPE Hydraulic Fracturing Technology Conference.

Kelkar, M. G. and Atiq, M. (2010). *Upgridding Method for Tight Gas Reservoirs*. Paper presented at the SPE Annual Technical Conference and Exhibition in Italy.

Klimentidis, R., Lazar, O. R. Bohacs, K. M., Esch, W. L., and Pedersen, P. (2010). *Integral Petrography of Mudstones*. Paper presented at the AAPG Annual Convention.

Klinkenberg, L. J. (1941). The Permeability of Porous Media to Liquids and Gases. *API Drilling and Production Practice*, 200-213.

Knudsen, M. (1909). Die Gesetze der Molekularströmung und der inneren Reibungsströmung der Gase durch Röhren (The Laws of Molecular and Viscous Flow of Gases Through Tubes). *Annalen der Physik*, **333**(1), 75-130.

LaFollette R. F., Carman P. S. (2010). *Proppant diagenesis: Results So Far.* Paper presented at the SPE unconventional gas conference.

LeVeque, R. J. (2002). *Finite volume methods for hyperbolic problems* (Vol. 31): Cambridge university press.

Loucks, R. G., Reed, R. M., Ruppel, S. C., and Jarvie, D. M. (2009). Morphology, Genesis, and Distribution of Nanometer-Scale Pores in Siliceous Mudstones of the Mississippian Barnett Shale. *Journal of Sedimentary Research,* **79**(12), 848-861.

Lu, X. C., Li, F. C. and Watson, A. T. (1995). Adsorption Studies of Natural Gas Storage in Devonian Shales. *SPE Formation Evaluation,* **10**(2), 109-113.

Mengal, S.A. and Wattenbarger, R.A. (2011). *Accounting for Adsorbed Gas in Shale Gas Reservoirs*. Paper presented at the SPE Middle East Oil and Gas Show and Conference in Bahrain.

Moradis, G. J., Blasingame, T. A., and Freeman, C. M. (2010). *Analysis of Mechanisms of Flow in Fractured Tight-Gas and Shale-Gas Reservoirs*. Paper presented at the SPE Latin American and Caribbean petroleum engineering conference.

P. H. Forchheimer. (1901). Wasserbewegung Durch Boden (Movement of Water Through Soil). *Zeitschr Ver Deutsch Ing*, **49**, 1736-1749.

Passey, Q. R., Bohacs, K., Esch, W. L., Klimentidis, R., and Sinha, S. (2010). *From Oil-Prone Source Rock to Gas-Producing Shale Reservoir – Geologic and Petrophysical Characterization of Unconventional Shale Gas Reservoirs*. Paper presented at the CPS/SPE International Oil & Gas Conference and Exhibition in China.

Peaceman, D. W. (1977). Fundamentals of Numerical Reservoir Simulation. *Developments in Petroleum Science*, **6**, page 2

Pope C, Benton T, Palisch T. (2009). *Haynesville Shale-One Operator`s Approach to Well Completions in This Evolving Play*. Paper presented at the SPE annual technical conference and exhibition.

Raghavan, R. and Chin, L. Y. (2004). Productivity Changes in Reservoirs with Stress-Dependent Permeability. *SPE Reservoir Evaluation & Engineering*, **7**(4), 308-315.

Roy, S., Raju, R., Chaung, H. F. et al. (2003). Modeling Gas Flow Through Microchannels and Nanopores. *Journal of Applied Physics*, **93**(8), 4870-4879.

Rubin B. (2010). *Accurate Simulation of Non-Darcy Flow in Stimulated Fractured Shale Reservoirs*. Paper presented at the SPE western regional meeting in California.

Rutqvist, J. Y., Wu, S., Tsang, C. F., Bodvarsson, G. (2002). A Modeling Approach for Analysis of Coupled Multiphase Fluid Flow, Heat Transfer, and Deformation in Fractured Porous Rock. *International Journal of Rock Mechanics and Mining Sciences*, **39**(4), 429-442.

Sakhaee-Pour, A. and Bryant, S. L. (2012). Gas Permeability of Shale. *SPE Reservoir Evaluation & Engineering*, **15**(4), 401-409.

Shabro, V., Torres-Verdin, C., and Javadpour, F. (2011). *Numerical Simulation of Shale-Gas Production: From Pore-Scale Modeling of Slip-Flow, Knudsen Diffusion, and Langmuir Desorption to Reservoir Modeling of Compressible Fluid.* Paper presented at the North American Unconventional Gas Conference and Exhibition.

Sherman, F. (1969). The Transition from Continuum to Molecular Flow. *Annual Review of Fluid Mechanics*, **1**, 317-340.

Sigal, R. F. (2013). *The Effects of Gas Adsorption on Storage and Transport of Methane in Organic Shales*. Paper presented at the SPWLA 54th Annual Logging Symposium.

Soeder, D. J. (1988). Porosity and Permeability of Eastern Devonian Gas Shale. *SPE Formation Evaluation*, **3**(1), 116-124.

Sondergeld, C. H., Ambrose, R. J. Rai, C. S., and Moncrieff, J. (2010a). *Micro-Structural Studies of Gas Shales*. Paper presented at the SPE Unconventional Gas Conference.

Sun, J. and Schechter, D. (2015a). Optimization-Based Unstructured Meshing Algorithms for Simulation of Hydraulically and Naturally Fractured Reservoirs with Variable Distribution of Fracture Aperture, Spacing, Length and Strike. *SPE Reservoir Evaluation & Engineering*, **18(**40), 463-480.

Sun, J. and Schechter, D. (2015b). Investigating the Effect of Improved Fracture Conductivity on Production Performance of Hydraulic Fractured Wells through Field Case Studies and Numerical Simulations. *Journal of Canadian Petroleum Technology*, **54**(6), 442-449.

Swami, V. and Settari, A. (2012). *A Pore Scale Gas Flow Model for Shale Gas Reservoir.* Paper presented at the Americas Unconventional Resources Conference.

Wang F. P. and Reed, R. M. (2009). *Pore Networks and Fluid Flow in Gas Shales*. Paper presented at the SPE annual technical conference and exhibition.

Wang, H. and Marongiu-Porcu, M. (2015). Impact of Shale-Gas Apparent Permeability on Production: Combined Effects of Non-Darcy Flow/Gas-Slippage, Desorption, and Geomechanics. *SPE Reservoir Evaluation & Engineering*, **18**(4), 495-507.

Wang, J., Luo, H. Liu, H., Cao, F., Li, Z., Sepehrnoori, K. (2017). An Integrative Model to Simulate Gas Transport and Production Coupled with Gas Adsorption, Non-Darcy Flow, Surface Diffusion, and Stress-Dependence in Organic-Shale Reservoirs. *SPE Journal*, **22**(1), 244-264.

Warpinski, N. R., Mayerhofer, M., Agarwal, K., and Du, J. (2013). Hydraulic Fracture Geomechanics and Microseismic-Source Mechanisms. *SPE Journal* **18**(4), 766-780.

Wasaki, A. and Akkutlu, I. Y. (2014). *Permeability of Organic-rich Shale.* Paper presented at the SPE Annual Technical Conference and Exhibition.

Winterfeld, P. H. and Wu, Y. S. (2011). *Parallel Simulation of CO2 Sequestration with Rock Deformation in Saline Aquifers*. Paper presented at the SPE Reservoirs Simulation Symposium.

Wu, K., Li, X., Guo, C. et al. (2015). *Adsorbed Gas Surface Diffusion and Bulk Gas Transport in Nanopores of Shale Reservoirs with Real Gas Effect-Adsorption-Mechanical-Coupling.* Paper presented at the SPE Reservoir Simulation Symposium.

Wu, Y. S., Pruess, K., and Persoff, P. (1998). Gas Flow in Porous Media with Klinkenberg Effects. *Transport in Porous Media*, **37**, 117-137.

Wu, Y. S., Li, J., Ding, D., Wang, C., and Di, Y. (2014). A Generalized Framework for the Simulation of Gas Production in Unconventional Gas Reservoirs. *SPE Journal*, **19**(5).

Xiong, X., Devegowda, D., Michel, G. G. et al. (2012). *A Fully-Coupled Free and Adsorptive Phase Transport Model for Shale Gas Reservoirs Including Non-Darcy Flow Effects.* Paper presented at the SPE Annual Technological Conference and Exhibition.

Yang, F., Ning, Z., Hu, C., Wang, B., Peng, K., and Liu, H. (2013). Characterization of Microscopic Structures in Shale Reservoirs. *Acta Petrolei Sinica*, **34**(2), 301-311.

Yu, W. and Sepehrnoori, K. (2014). Simulation of Gas Desorption and Geomechanics Effect for Unconventional Gas Reservoirs. *Fuel*, **116**, 455 – 464.

Yu, W., Sepehrnoori, K. and Patzek, T. W. (2014). *Evaluation of Gas Adsorption in Marcellus Shale*. Paper presented at the SPE Annual Technical Conference and Exhibition.

Zhang, J., Kamenov, A., Zhu, D., and Hill, A. D. (2014). Laboratory Measurement of Hydraulic-Fracture Conductivities in the Barnett Shale. *SPE Journal*, **29**(3),

Zhang, Z. Y. and Yang, S. B. (2012). On the Adsorption and Desorption Trend of Shale Gas. *Journal of Experimental Mechanics,* **27**(5), 492-497.

Ziarani, A. S. and Aguilera, R. (2011). Knudsen`s Permeability Correction for Tight Porous Media. *Transport in Porous Media*, **91**(1), 239-260.

Appendix

A) Initial and Current Gas in Place

From (29) we see that the mass concentration of gas (mass per volume) is related by a constant factor to the pressure formulation. This factor can be used to evaluate the recovery of gas:

(1) $$GOIP = \int_V \phi\rho_g + (1-\phi)a_g dV\,|_{\mathrm{P_{init}}}$$

This equation must be evaluated over the two sides of matrix. First consider the free gas:

(2) $$\rho_g(P_{g,0}) = \rho_{gs} b'_g P_{init}$$

The pore volume of free gas is:

(3) $$(2b_0 L_y)\phi^f + (2L_x L_y)\phi^m$$

Now consider the adsorbed gas:

(4) $$a_g(P_{init}) = a_{max}\left(\frac{P_{init}}{P_{init}+P_L}\right)$$

The bulk volume of the matrix, where adsorbed gas is located, is given by:

(5) $$(2L_x L_y)$$

Adding the various contribution, the gas originally in place is:

(6) $$GOIP = \left[(2b_0 L_y)\phi^f + (2L_x L_y)\phi^m\right]\rho_g(P_{init}) + (2L_x L_y)a_g(P_{init})$$

where b_0 is the average fracture width. Since height is not accounted for, GIP will actually have unit of mass per height, but a unit height can be assumed.

The gas currently in place (GCIP) is the sum of the adsorbed gas in the matrix (mass1), the free gas in the fracture (mass2) and the free gas in the matrix (mass3). It can be calculated as follows:

$$mass1 = 2\int_{x=0}^{x=L_x}\int_{y=0}^{y=L_y}(1-\phi^m)a_g\left(P_g(x,y)\right)dxdy \tag{7}$$
$$= 2\sum_{i=0}^{i=n_x}\sum_{j=0}^{j=n_y}(1-\phi^m)a_g\left(P_g(x_i,y_i)\right)\Delta x\Delta y$$

Note that the expression is only integrated over the right side of the fracture and then multiplied by 2 to account for the matrix located on the left side.

$$mass2 = \int_V \phi\rho_g dV$$
$$= \int_{x=-2b(y)}^{x=0}\int_{y=0}^{y=L_y}\phi\rho_g dxdy \tag{8}$$
$$= \int_{x=-2b(y)}^{x=0}\int_{y=0}^{y=L_y}\phi^f\rho_{gs}b'_g P_g(x,y)dxdy$$
$$= \sum_{j=1}^{j=n_y}\phi^f\rho_{gs}b'_g \mathrm{P_g(y_j)2b(y_j)}\Delta y$$

Note that $2b(y_j)$ is the average width of cell nr j.

$$mass3 = \int_V \phi\rho_g dV$$
$$= 2\int_{x=0}^{x=L_x}\int_{y=0}^{y=L_y}\phi\rho_g dxdy \tag{9}$$
$$= 2\int_{x=0}^{x=L_x}\int_{y=0}^{y=L_y}\phi^m\rho_{gs}b'_g P_g(x,y)dxdy$$
$$= 2\sum_{j=1}^{j=n_y}\phi^m\rho_{gs}b'_g \mathrm{P_g(i,j)}\Delta \mathrm{x}\Delta y$$

The GCIP is then:

$$GCIP = mass1 + mass2 + mass3 \tag{10}$$

B) Operator splitting

The scaled transport system (65) and (66) is solved using an operator splitting approach similar to that presented in Berawala et al. 2018, Andersen et al. (2014; 2015) and Andersen et al. (2016). The coupled system is split into the two following subsystems (the ´notation has been dropped):

a. Fracture diffusion. Flow in the y-direction.

Set $\partial_x P = 0$ and $\partial_t \hat{a}_g = 0$:

$$b(y)\partial_t(P\phi^f) = \partial_y\left(DbK^f\partial_y P\right) \qquad \left(x, y \in \Omega^{\mathrm{f}}\right)$$

$$\partial_t G = 0 \qquad (x, y \in \Omega^m)$$

b. Fracture-matrix diffusion and desorption. Flow in the -direction.

Here we have no flow in the y-direction, so we set $\partial_y P = 0$.

$$b(y)\partial_t(P\phi^f) = \alpha\beta(DK^m\partial_x P)_{x=0,y} \qquad \left(x, y \in \Omega^{\mathrm{f}}\right)$$

$$\partial_t G = \alpha\partial_x(DK^m\partial_x P) \qquad (x, y \in \Omega^m)$$

This system is further split into two subsystems where we 1) only consider diffusion with adsorbed mass held fixed and 2) equilibrate adsorbed mass with pressure in the matrix.

We apply the Strang splitting approach so that that system a is solved during the time $\Delta t/2$, then system b is solved during the time Δt before system a is solved for time $\Delta t/2$ again. The splitting step, Δt, must be selected sufficiently small to allow the different systems to participate frequently enough to provide relevant information in each others solution procedure.

Fracture-matrix diffusion. With no desorption we set $\partial_t \hat{a}_g = 0$ and solve the diffusion system:

$$b(y)\partial_t(P\phi^f) = \alpha\beta(DK^m\partial_x P)_{x=0,y} \qquad \left(x, y \in \Omega^{\mathrm{f}}\right)$$

$$\partial_t G = \alpha\partial_x(DK^m\partial_x P) \qquad (x, y \in \Omega^m)$$

Desorption. No flow in x-direction or y-direction, so we set $\partial_x P = 0$ and $\partial_y P = 0$.

$$b\partial_t(P) = 0 \qquad \left(x, y \in \Omega^{\mathrm{f}}\right)$$

$$\partial_t G = 0 \qquad (x, y \in \Omega^m)$$

This means that we have no flow, but locally we adjust P, $\hat{a}(P)$ and ϕ^m to be in equilibrium. The conserved property is:

$$G = \phi^m\left(P_g + \hat{a}_g\right)$$

Since pressure has been diffused without changes to $\hat{a}_g$, the pressure and $\hat{a}_g$ are not in equilibrium and require adjustment. At equilibrium we have an adjusted pressure P_{eq} and corresponding adsorbed content $\hat{a}_g(P_{eq})$ which must add up to the same amount G:

$$G = \phi^m\left(P_{eq} + \hat{a}_{max}\left(\frac{P_{eq}}{P_{eq} + P_L}\right)\right)$$

This can be written:

$$\phi^m P_{eq}^2 + (\phi^m P_L + \phi^m \hat{a}_{max} - G)P_{eq} - GP_L = 0$$

This is a quadratic formula which gives:

$$P_{eq} = \frac{-(\phi^m P_L + \phi^m \hat{a}_{max} - G) \pm \sqrt{(\phi^m P_L + \phi^m \hat{a}_{max} - G)^2 + 4\phi^m G P_L}}{2\phi^m}$$

This value is then scaled and returned from the adsorption-correction.

C) Discretization

Assume the y-axis is discretized into j = 1:N_y cells and the matrix (not including the fracture) into i = 1:N_x cells.

a. *Fracture diffusion*. We only consider the fracture, no changes in the matrix.

$$b(y)\partial_t(P\phi^f) = \partial_y\left(Db(y)K^f\partial_y P\right) \qquad \left(x, y \in \Omega^{\mathrm{f}}\right)$$

The scaled (half) width $b(y)$ varies generally, but for a given cell j b_j is constant. The conserved property is P, which integrated over the grid cell gives:

$$\frac{b_j(P_j^{n+1}\phi_j^{f,n+1} - P_j^n\phi_j^{f,n})}{\Delta t} = \frac{\left(Db(y)K^f\partial_y P\right)_{j+\frac{1}{2}} - \left(Db(y)K^f\partial_y P\right)_{j-\frac{1}{2}}}{\Delta y} \qquad \left(x, y \in \Omega^{\mathrm{f}}\right)$$

This scheme will conserve mass regardless of flux. The flux is selected as:

$$\left(Db(y)K^f\partial_y P\right)_{j+\frac{1}{2}} = \frac{D_{j+1} + D_j}{2}\frac{b_{j+1} + b_j}{2}\frac{K_{j+1}^f + K_j^f}{2}\frac{P_{j+1} - P_j}{\Delta y}$$

If we assume that the porosity is constant over the time step and can be calculated using the pressure at the previous time step, we get:

$$\frac{b_j\phi_j^{f,n}(P_j^{n+1} - P_j^n)}{\Delta t} = \frac{\left(Db(y)K^f\partial_y P\right)_{j+\frac{1}{2}} - \left(Db(y)K^f\partial_y P\right)_{j-\frac{1}{2}}}{\Delta y}$$

And then:

$$P_j^{n+1} = \frac{\Delta t\left(Db(y)K^f\partial_y P\right)_{j+\frac{1}{2}} - \left(Db(y)K^f\partial_y P\right)_{j-\frac{1}{2}}}{\mathrm{b_j}\,\phi_j^{f,n}\Delta y} + P_j^n$$

b. *Fracture-matrix diffusion.* With no desorption we set $\partial_t \hat{a}_g = 0$ and solve the diffusion system:

$$b(y)\partial_t(P\phi^f) = \alpha\beta(DK^m\partial_x P)_{x=0,y} \qquad \left(x, y \in \Omega^{\mathrm{f}}\right)$$

$$\partial_t G = \alpha\partial_x(DK^m\partial_x P) \qquad (x, y \in \Omega^m)$$

For the central cells in the matrix we have:

$$\frac{P_i^{n+1}\phi_i^{m,n+1} - P_i^n\phi_i^{m,n}}{\Delta t} = \alpha\frac{(DK^m\partial_x P)_{i+1/2} - (DK^m\partial_x P)_{i-1/2}}{\Delta x}$$

At the fracture-matrix interface we have:

$$b_j\frac{P_0^{n+1}\phi_0^{f,n+1} - P_0^n\phi_0^{f,n}}{\Delta t} = \alpha\beta(DK^m\partial_x P)_{i=\frac{1}{2},j} \qquad \left(x, y \in \Omega^{\mathrm{f}}\right)$$

$$\frac{P_i^{n+1}\phi_i^{m,n+1} - P_i^n\phi_i^{m,n}}{\Delta t} = \alpha\frac{(DK^m\partial_x P)_{i=\frac{3}{2},j} - (DK^m\partial_x P)_{i=\frac{1}{2},j}}{\Delta x} \qquad (x, y\,\epsilon\Omega^m)$$

The fracture-matrix flux term is evaluated by:

$$(DK^m\partial_x P)_{i=\frac{1}{2},j} = \frac{D_{0+}D_1}{2}\frac{K_0^m + K_1^m}{2}\frac{P_1 - P_0}{\left(\frac{\Delta x}{2}\right)}$$

The pressure gradient assumes the fracture pressure is given at the interface and not at the fracture center.